

1 **Assimilation of snow water equivalent from AMSR2 and IMS**
2 **satellite data utilizing the local ensemble transform Kalman filter**

3
4 Joonlee lee¹, Myong-In Lee^{1*}, Sunlae Tak¹, Eunkyo Seo^{2,3} and Yong-Keun ~~Lee~~³Lee⁴

5
6 ¹ *Department of Civil, Urban, Earth, and Environmental Engineering, Ulsan National*
7 *Institute of Science and Technology, Ulsan, Korea*

8 ² *Department of Environmental Atmospheric Sciences, Pukyong National University, Busan,*
9 *South Korea.*

10 ^{3,3} *Center for Ocean-Land-Atmosphere Studies, George Mason University, Fairfax, VA, USA*

11 ⁴ *Earth System Science Interdisciplinary Center, University of Maryland, College Park,*
12 *U.S.A.*

13
14
15
16 NOV 15, 2023

17
18
19
20 To be submitted to GMD

21
22

*Corresponding author: Prof. Myong-In Lee, Department of Urban and Environmental

- 23 Engineering, Ulsan National Institute of Science and Technology, 50 UNIST-gil, Ulsan 44919,
- 24 Republic of Korea (milee@unist.ac.kr)

25 Abstract

26 ~~The Snow Water Equivalent (SWE), as one of the land initial conditions, plays a crucial~~
27 ~~role in global or regional energy and water balance, thereby exerting a considerable impact on~~
28 ~~seasonal and sub-seasonal scale predictions owing to its enduring memory over 1 to 2 months.~~
29 ~~Despite its importance, most SWE initialization remains challenging due to its reliance on~~
30 ~~simple approaches based on spatially constrained observation. Therefore, this study developed~~
31 ~~the advanced snowSWE data assimilation is developed in this study framework~~ with satellite
32 remote-sensing ~~retrievals of snow water equivalent(SWE) and snow cover fraction(SCF) data~~
33 utilizing the local ensemble transform Kalman filter ~~based on(LETKF) and~~ the Joint U.K. Land
34 Environment Simulator (JULES) land model. ~~The system assimilates SWE. This constitutes a~~
35 ~~novel approach that has not been previously attempted, as it offers an objective way to~~
36 ~~optimally combine two imperfect data sources: the satellite SWE retrieval~~ from the Advanced
37 Microwave Scanning Radiometer 2(AMSR2) ~~and SCF (AMSR2) and dynamically balanced~~
38 ~~SWE from JULES land model. In this framework, an algorithm is additionally considered to~~
39 ~~determine the assimilation process based on the presence or absence of snow cover~~ from the
40 Interactive Multisensor Snow and Ice Mapping System (IMS) ~~during April 2013-2020. The~~
41 ~~performance is evaluated by the validations with independent data assimilation products~~
42 ~~derived from in situ observations~~ satellite, renowned for its superior reliability.

43 The baseline model simulation from JULES without satellite data assimilation shows a
44 superior performance in high-latitude regions with heavy snow accumulation, but relatively
45 inferior in the transition regions with less snow and high spatial and temporal variation.
46 Contrastingly, the AMSR2 satellite data exhibit ~~a superior~~ better performance in the transition
47 regions, but ~~poor performance~~ poorer in the high latitudes, presumably due to the limitation of
48 ~~the satellite data~~ in the penetrating depth ~~of satellite retrieval.~~ The data assimilation(DA) ~~that~~
49 ~~combines AMSR2 and IMS satellite data with the JULES model backgrounds (DA)~~

50 demonstrates the positive impacts by reducing uncertainty in ~~both satellite-derived snow data~~
51 ~~in penetrating deep snow and~~ the JULES model simulations in ~~the transition regions~~. While
52 ~~DA shows superior performance in most regions, it specifically improves the analysis areas,~~
53 particularly in the mid-latitude transition regions ~~where~~. In the transition regions, the model
54 background errors from the ensemble runs are significantly larger than the observation errors,
55 emphasizing ~~the substantial influence of satellite information~~. ~~The long-term analysis of snow~~
56 ~~manifests a pronounced variability in the continental interior at the interannual timescales,~~
57 ~~which implies large uncertainty in the snow initialization for the sub-seasonal to seasonal~~
58 ~~predictions of the climate models, potentially degrading prediction skills without satellite snow~~
59 ~~data assimilation~~. great uncertainty in the model simulations. The results of this study highlight
60 the beneficial impact of data assimilation by effectively combining both land surface model
61 and satellite-derived data according to their relative uncertainty, thereby controlling not only
62 transitional regions but also satellite-constrained areas experiencing heavy snow accumulation.
63 This assimilation framework is anticipated to contribute to a more precise prediction of
64 atmospheric conditions by realistically capturing the interaction between the atmosphere and
65 land, given the substantial influence of SWE on energy and water balance at the interface of
66 the atmosphere and land.

67

68 1. Introduction

69 Snow plays a crucial role in regulating the water, energy, and carbon exchange between the
70 land surface and atmosphere (e.g., Dutra et al., 2011; Thomas et al., 2016). A snowpack tends
71 to increase surface albedo and soil moisture as the snow melts. ~~It has an impact on~~
72 ~~(Eagleson, 1970), thereby affecting~~ the climate system ~~with the~~ through changes in water
73 ~~balance by the soil moisture change and the energy~~ balance by albedo variations balances. In
74 addition to local impacts, the continental snowpack over Eurasia can influence the large scale
75 atmospheric circulation during winter (e.g., Li and Wang, 2014) or in spring (e.g., Broxton et
76 al., 2017). ~~Especially~~ Especially, the Eurasian autumn snow can affect upward-propagating
77 stationary Rossby-wave activity, leading to stratospheric warming and weakening of
78 stratospheric polar vortex and jet stream, which in turn emerges as a negative Arctic oscillation
79 (AO)-like pattern at the surface during winter due to downward propagation through the
80 troposphere. Its impact is shown in both observation and model experiments (e.g., Allen and
81 Zender 2011; Cohen et al. 2007). ~~Therefore~~ Furthermore, the interannual variability of snow
82 ~~initialization process in climate models is closely related to melting during~~ the improvement of
83 prediction performance. boreal spring season affects surface soil moisture in summer, which
84 has important implications for heatwave development and emphasizing mechanisms through
85 land-atmosphere interactions (Seo et al., 2020).

86 In the ~~short and medium forecasts, snow is simply prescribed based on~~
87 ~~climatological values because the forecasts are significantly influenced by the accuracy of the~~
88 ~~initial atmospheric states in climate models. To extend the accurate prediction to~~ subseasonal
89 to seasonal (S2S) timescales, ~~the atmospheric and the more slowly evolving initial conditions~~
90 ~~need to be carefully considered. Land initial states such as snow~~ land initial states are crucial
91 components in the S2S timescale predictions due to ~~their climatic~~ the inherent memory
92 ~~lasting~~ that changes slowly for 1- to 2 months in the climate system (e.g., Derome et al. 2005;

93 Chen et al., 2010). ~~The~~; Seo et al., 2019). In particular, ~~the~~ realistic snow initial states ~~can~~
94 contribute to improving S2S prediction skills, as proven in several modeling studies ~~(e.g.,~~ For
95 example, previous studies (Orsolini et al., 2013; Jeong et al., 2013) demonstrated a
96 considerable enhancement in prediction skill of 2m air temperature up to a lead time of 1-2
97 months across certain regions of Eurasia and the Arctic during winter, depending on snow
98 initialization. Moreover, other studies (Orsolini et al., 2016; Li et al., 2019);2019) have
99 revealed that wave activity propagating toward the stratosphere, influenced by snow initial
100 conditions in climate models, can induce changes in the polar vortex and contribute to the
101 persistence of the North Atlantic Oscillation (NAO) and the AO. This emphasizes the
102 significance of snow initialization in climate models as an essential process for enhancing
103 prediction performance at the S2S timescales.

104 Snow states Snow states, i.e., snow water equivalent (SWE) used directly for hydrological
105 analysis and initial states of the model (Li et al., 2019; Gan et al., 2021), are generally provided
106 from in-situ observations data, remote-sensing retrievals from satellites, or numerical models
107 such as the land surface model (LSM) operated based on the observed atmospheric variables.
108 ~~In the case of~~ For the in-situ data, ~~the primary source of~~ snow depth (SD) ~~is obtained from~~
109 ~~surface~~ measurements prevail, largely attributed to the challenges associated with acquiring
110 precise SWE data (Takala et al., 2011; De Rosnay et al., 2014). Surface synoptic observations
111 ~~(SYNOP). These observations are provided almost in real time through the global~~
112 ~~telecommunication system(GTS). In addition to SYNOP, there are some regional snow~~
113 ~~measurement networks. For instance, the snowpack telemetry(SNOTEL) network collects data~~
114 ~~on) serve as the principal source for SD over 900 automated observation points located in the~~
115 ~~western United States, and the National Oceanic and Atmospheric Administration (NOAA)~~
116 ~~Cooperative Observer Program gathers SD data in North American region. Nevertheless, data~~
117 ~~collected from these national networks cannot be utilized in the almost real time GTS. Directly~~

118 ~~measured measurements. The in-situ data provide measurements offer~~ the most
119 ~~reliable dependable~~ snow information ~~but have, yet they are characterized by~~ relatively coarse
120 temporal and spatial resolutions ~~over the, particularly within~~ limited ~~area because of areas, due~~
121 ~~to the~~ spatial ~~heterogeneities of snow~~ heterogeneity inherent in snow distribution. (Helmert et
122 al., 2018). ~~Recently, in order to obtain high resolution and high quality snow water~~
123 ~~equivalent(SWE) analysis, artificial intelligence(AI) such as long short term memory(LSTM)~~
124 ~~has been utilized with the given meteorological conditions from SNOTEL observations as input~~
125 ~~data, but it is still insufficient to cover the entire globe(;~~ Meyal et al., 2020).

126 Satellite-derived observations using conical scanning microwave instruments may
127 provide spatially consistent data coverage across the globe. Cho et al. ~~(.~~ (2017) showed the SWE
128 retrieval results from two passive microwave sensors, the advanced microwave scanning
129 radiometer 2 (AMSR2) and the special sensor microwave imager sounder (SSMIS). However,
130 the algorithms for SWE retrieval exhibit a degree of sensitivity to a variety of parameters such
131 as snow liquid water content and snow grain size distribution (De Rosnay et al., 2014). Hence,
132 satellite-based SWE data still have limitations in accuracy, especially under deep snow
133 conditions due to the ~~restrictions in limited~~ penetration depth (Gan et al., 2021). On the other
134 hand, satellite retrieval can estimate snow cover accurately under clear sky conditions
135 (Brubaker et al., 2009). ~~The moderate resolution imaging spectroradiometer(MODIS)~~
136 ~~instrument observes daily snow cover, while a multi-satellite-based interactive multi-sensor~~
137 ~~snow and ice mapping system(IMS) provided by the United States National Snow and Ice Data~~
138 ~~Center produces the snow cover by combining in situ observations and satellite data from~~
139 ~~microwave, infrared, and visible sensors.~~

140 Model simulations obtained from LSMs and simple snow models can cover complete
141 spatiotemporal resolution but involve potentially large uncertainties due to the deficiencies in
142 the physical parameterizations and meteorological forcing data (Dirmeyer et al., 2006; Seo et

143 al., 2020). ~~To reduce the uncertainties from model simulations, previous studies have used~~
144 ~~satellite-based~~ 2021).

145 Considering that snow cover and in-situ observation datasets have their respective strengths
146 as well as limitations, data assimilation or other data fusion methods can prove to be beneficial
147 for constructing snow states such as ~~SYNOP SD available on the GTS, in conjunction with the~~
148 ~~model simulation~~ reanalysis data (e.g., Brasnett, 1999; Dee et al., 2011; Meng et al., 2012;
149 Pullen et al., 2011; De Rosnay et al., 2014). For example, the snow analysis for the Canadian
150 Meteorological Center (CMC) utilizes a 2-dimensional optimal interpolation (2D-OI) scheme
151 with in-situ observations and the outputs from a simple snow model (Brown et al., 2003). The
152 National Centers for Environmental Prediction (NCEP) climate forecast system reanalysis
153 (CFSR) combines ~~the~~ a multi-satellite-based interactive multi-sensor snow and ice mapping
154 system (IMS) as satellite-based snow cover retrieval and the outputs from the global ~~SD~~ snow
155 model of the Air Force Weather Agency (Meng et al., 2012). At the European Center for
156 Medium Weather Forecast (ECMWF), the ECMWF reanalysis (ERA)-Interim and ERA5 for
157 the snow analysis employ a Cressman interpolation and 2D-OI, respectively, with the IMS, in-
158 situ observation, and the results from a land surface model (Dee et al. 2011; De Rosnay et al.,
159 2014). The Japanese 55-year Reanalysis (JRA55) also utilizes the 2D-OI with in-situ
160 observation, satellite-based snow cover from SSMIS, and the results from an LSM (~~Kobayashi~~
161 ~~et al., 2015).~~ (Kobayashi et al., 2015). Given that the majority of the reanalysis datasets rely on
162 snow depth measurements, the SWE estimation is likely to introduce potential accuracy
163 concerns when the snow depth information is combined with the snow density calculations.

164 ~~The most commonly employed approach to obtain reasonable estimates of land initial states~~
165 ~~for predictions is running atmospheric general circulation models (AGCMs; Pullen et al., 2011)~~
166 ~~or offline mode of LSMs with observed atmospheric conditions (Dirmeyer et al., 2006).~~ Climate
167 prediction systems in operational centers such as the Meteorological Office (~~Met Office~~) (Met

168 Office) in the United Kingdom and the Korean Meteorological Administration (KMA) conduct
169 the snow initialization by utilizing the results of the operational global unified model (UM) and
170 the IMS snow cover, which solely indicates the presence of snow (Pullen et al., 2011), lacking
171 in its ability to reflect the physical quantity of it. The initialization at NCEP also performs a
172 similar approach using input data combined from IMS snow cover and results from the global
173 SD model (SNODEP; Meng et al., 2012). Furthermore, the snow initialization of ECMWF
174 employs optimal interpolation with a combination of results from the LSM, IMS snow cover,
175 and in-situ observation from SYNOP and national networks available on the GTS. However,
176 in areas/regions where ground observations are not available, the results of unavailable, large
177 errors may exist in the snow model are relied upon, which still exists significant uncertainty in
178 snow accumulation because of outputs due to uncertainties in the atmospheric forcing and
179 imperfect model parameterizations/parameterization (Boone et al., 2004; Essery et al., 2009). It
180 would be useful to to accurately initialize the Often, the snow processes parameterized in LSMs
181 rely on observed properties sampled in limited areas (Lim et al., 2022). In addition, as IMS
182 snow amount including vertical depth, which is more important in estimating energy and water
183 budgets, by using cover only identifies the presence of snow, the data assimilation with the
184 satellite-derived snow amounts with comparatively uniform spatial snow cover only is not
185 sufficient and inappropriate in constraining water and temporal resolution/energy conservation.
186 Alternative methods that consider the physical quantity of snow are required for the snow
187 initialization.

188 One approach to mitigate the spatial discontinuity of ground observations is to use satellite-
189 derived SWE with wide spatial coverage and frequent temporal resolution. However, the SWE
190 retrievals from satellites still have considerable uncertainties (De Lannoy et al., 2010; Dawson
191 et al., 2018), which can arise from vegetation and terrain interference, sensor signal saturation,
192 snowfall amount, and simplifications in the underlying assumptions of the retrieval algorithms

193 (Liu et al., 2015). In particular, a region with heavy snow accumulation leads to a significant
194 underestimation of SWE due to the limitations in penetration depth from satellites_(Gan et al.,
195 2021).~~For this reason, so that~~ satellite-derived SWE is not employed in the land initialization
196 process.~~Nevertheless, the SWE retrieval shows important advantages such as high~~
197 ~~performance in shallow snow areas with temporal and spatial homogeneity(Gan et al., 2021).~~
198 In previous studies, various approaches have been attempted to improve SWE product
199 performance, such as combining satellite-derived SWE with ground observations_(Pulliainen
200 et al., 2020), different satellite data sets_(Gan et al., 2021), simple snow models_(Dziubanski
201 and Franz, 2016), or LSMs_(Kwon et al., 2017).~~For instance, Kumar et al.(., 2019) show the~~
202 ~~improvement of the SD estimation over the contiguous United States by assimilating satellite~~
203 ~~snow SD into the Noah LSM, indicating that these model).~~ However, most previous studies
204 ~~have focused on targeted regions with limited ground-based products are generally superior to~~
205 ~~stand-alone satellite-based SWE retrievals. Thus, a globally advanced snow observations. Snow~~
206 initialization ~~such as data assimilation in global coverage using satellite snow amount is ideal~~
207 ~~for providing realistic snow initial states related to S2S prediction skills-derived SWE remains~~
208 ~~a persistently challenging task.~~

209 Therefore, ~~the purpose of this study is to develop~~developed an advanced ~~snow~~SWE data
210 assimilation ~~system utilizing the Local Ensemble Transform~~framework with satellite remote-
211 sensing data using the local ensemble transform Kalman ~~Filter~~filter (LETKF) ~~with satellite-~~
212 ~~derived observations of SWE, IMS snow cover, as well as and~~ the Joint U.K. Land
213 Environment Simulator(JULES). ~~In this context, our focus is on SWE rather than SD, because~~
214 ~~the former can be used directly for hydrological analysis and initial states of the model(Gan et~~
215 ~~al., 2021). From this novel~~ (JULES) land model. This constitutes a novel approach that has
216 not been previously attempted, and it offers an objective way to optimally combine two
217 imperfect data sources: the satellite SWE from the Advanced Microwave Scanning Radiometer

218 2 (AMSR2) and the dynamically-balanced SWE from the JULES land model forced by
219 observed atmospheric fields. The estimated SWE data exhibit better consistence by
220 additionally using snow cover data from the IMS data. This assimilation system, we endeavor
221 to achieve the following objectives. The primary aim is to assess the enhancement in SWE
222 framework also enables the assessment of improvement as it provides insights into the reasons
223 behind the performance through the improvement based on the Kalman gain analysis that
224 measures the relative significance of the input data between the satellite and the land model
225 during the data assimilation with satellite remote sensing data cycle. The satellite data
226 show have demonstrated high performance reliability in the transition regions with of
227 climatologically shallow snow conditions, termed by Koster (Gan et al. (2004), 2021), and
228 these regions are known as "hot spots" of strong atmosphere-land coupling. The second goal
229 is to reveal the reason for skill improvement with the snow data assimilation, based on the
230 Kalman gain analysis that measures the ratio of the model errors with respect to the observation
231 errors, through snow melting and associated surface energy and water balance changes (Koster
232 et al., 2004; Dirmeyer, 2011; Huning and AghaKouchak, 2020). From these perspectives, it
233 would be possible important to know how much evaluate the satellite has affected impact of
234 satellites on the transition regions, and how the assimilation system deals with the regions of
235 as well as on the deep snow accumulation regions where the satellite has difficulty in accurate
236 retrieval. The final goal is to evaluate the advantages satellite retrievals are challenging.
237 Furthermore, the benefits of assimilating satellite retrievals in extreme extremely high-
238 temperature events, specifically over Eurasia such as the case in April 2020, over Eurasia, can
239 be elucidated. In this regard, we expect that the this snow data assimilation of framework with
240 satellite-derived snow information SWE can be an alternative to produce significant in
241 providing optimal snow initial states for improving the S2S prediction skill in the by global
242 climate models.



244 **2. Data and model**

245 **2.1. Satellite data**

246 The snow information including snow cover and SWE can be derived from satellite
247 measurements offering global coverage and high temporal as well as spatial resolution. For
248 data assimilation, this study uses SWE calculated from brightness temperature measurements
249 obtained by the AMSR2 on board the Japanese Aerospace Exploration Agency (JAXA) global
250 change observation mission-water_(GCOM-W) satellite. This AMSR2 Unified Level-3_(L3)
251 dataset offers daily estimation of SWE at 25 km resolutions from July 2012 to the present.
252 AMSR2 has a sensor designed to detect microwave radiation naturally emitted from the surface
253 and atmosphere, employing six frequency bands ranging from 6.9 to 89 GHz. Through this
254 conical scanning mechanism, AMSR2 can acquire day and night datasets with nearly constant
255 spatial resolution over more than 99% of the global coverage every two days. Comprehensive
256 explanations of AMSR2 characteristics are available in Imaoka et al.~~(~~(2010). AMSR2 is
257 selected for the assimilation because it produces more ~~skilled~~accurate results by assimilating
258 data from modern sensors_(e.g., AMSR2) compared to data from conventional sensors_(e.g.,
259 AMSR-E)~~(~~(Cho et al., 2017).

260 The widely used multisensor-derived snow cover is IMS (e.g., Ramsay 1998; Helfrich et
261 al., 2007) produced by NOAA the National Environmental Satellite Data and Information
262 Service (NESDIS) for the Northern Hemisphere from February 2004 to the present at 4 km
263 resolutions. This dataset is generated using various data products, including multi-satellite
264 images and in-situ observations (U.S. National Ice Center, 2008). Since IMS provides binary
265 (0: no snow or 1: snow covered) snow cover information, we transform the IMS snow cover at
266 4 km grids to the snow cover fraction (SCF) within a 50-km LSM grid by counting the snow
267 pixel number with a value of 1. A 50-km LSM grid is declared as snow-covered when more
268 than 50% of the 4km pixels within the grid are covered with snow. In this study, the application

269 of the assimilation process is determined based on IMS-based SCF, renowned for its superior
270 reliability (e.g., Brown et al., 2014). Further details will be described in Section 3.3.

272 **2.2. Reference data for SWE and SCF**

273 The CMC daily estimated SWE is used for verification. The SWE data is processed using
274 statistical interpolation between a background field derived from a simple snow model and in-
275 situ daily SD_(Brown and Brasnett, 2010). In detail, this dataset utilizes optimal interpolation
276 methods to acquire spatial SD from the in-situ data, involving SYNOP, special aviation reports
277 from the World Meteorological Organization_(WMO), and meteorological aviation reports
278 (METAR). In areas with scant in-situ data, a simple snow accumulation and melt model is
279 employed to create an optimal interpolation that estimates snowmelt and snowfall worldwide,
280 assuming the persistence of the snowpack mass between snowfall and melting events
281 (Brasnett, 1999). Although the average elevation of snow measurement stations used in CMC
282 is biased toward low elevations (< 400m), ~~leading to a potential~~potentially causing relative
283 negative biasbiases at ~~high~~higher elevations with heavy snow accumulation, the CMC dataset
284 is often considered the premier snow analysis accessible in the Northern Hemisphere_(Su et al.
285 2010) and has still been widely used to evaluate model outputs_(e.g., Reichle et al., 2011;
286 Reichle et al., 2017; Toure et al, 2018). Therefore, the SWE of CMC produced without the
287 satellite-derived data is selected for verification as an independent dataset for evaluating the
288 assimilated analysis with remote sensing snow retrievals. Since only daily SD analysis is
289 provided in CMC, it is converted to daily SWE based on the snow bulk density methods_(e.g.,
290 Sturm et al., 2010). It is available from 12 March 1998 to the present and offers comprehensive
291 coverage of the entire Northern Hemisphere with a horizontal resolution of 24 km. The SWE
292 of CMC at its native horizontal resolution is interpolated onto the LSM grid through local area
293 averaging.

3294 ~~The widely used multisensor derived snow cover is IMS(e.g., Ramsay 1998; Helfrich et~~
3295 ~~al., 2007) produced by NOAA the National Environmental Satellite Data and Information~~
3296 ~~Service(NESDIS) for the Northern Hemisphere from February 2004 to the present at 4 km~~
3297 ~~resolutions. This dataset is generated using various data products, including multi-satellite~~
3298 ~~images and in-situ observations(U.S. National Ice Center, 2008). Since IMS provides binary(0:~~
3299 ~~no snow or 1: snow covered) snow cover information, we transform the IMS snow cover at 4~~
3300 ~~km grids to the snow cover fraction(SCF) within a 50 km LSM grid by counting the snow pixel~~
3301 ~~number with a value of 1. A 50 km LSM grid is declared as snow covered when more than 50%~~
3302 ~~of the 4km pixels within the grid are covered with snow. In this study, the IMS based SCF is~~
3303 ~~employed to mask the SWE, considering the higher reliability of IMS data (e.g., Brown et al.,~~
3304 ~~2014).~~

3306 **2.3. JULES LSM**

3307 This study utilizes the JULES LSM from the Met Office_(Best et al., 2011), a component
3308 land model of the global seasonal forecasting system version 6_(GloSea6) global, fully-coupled
3309 atmosphere, ocean, land, and sea-ice model. The surface types_(or snow tiles) in the JULES
3310 LSM consist of four non-vegetated types: urban, land-ice, inland water, and bare soil, as well
3311 as five vegetation functional types: C3 temperate grass, needleleaf trees, shrubs, C4 tropical
3312 grass, and broadleaf trees. For each surface tile, a separate energy balance is computed, and the
3313 average energy balance in the grid cells is determined by applying weights to the values of each
3314 surface tile. Two schemes are used within JULES to represent surface snow_(e.g., Best et al.,
3315 2011; Burke et al., 2013). The simple method involves a zero-layer approach, which modifies
3316 the top soil level without using explicit model layers to represent snow processes. The other is
3317 the multi-layer approach which is more comprehensive_, described in Best et al. (2011). In the
3318 case of vegetated surfaces, snow can be separated into ground snow and canopy snow or stored

319 in a single effective reservoir. As both the zero-layer and multi-layer snow models provide
320 similar results under various conditions (e.g., (Best et al., 2011), this study used the zero-layer
321 snow model with constant thermal conductivity and density for snow. Although the heat
322 capacity of snow is ignored, the bulk thermal conductivity in the surface layer is reduced as the
323 thermal conductivity of snow differs from that of the soil and the layer thickness increases. As
324 long as snow persists on the ground, the skin temperature cannot exceed 0°C, yet the heat flux
325 utilized for melting the snow is diagnosed ~~through~~ as the residual in the surface energy balance.
326 The melted water is immediately drained from the snow, divided into runoff and soil infiltration,
327 and liquid water is not stored or frozen in the snow. A detailed description of the energy and
328 water cycling in the JULES LSM can be referenced in Best et al. ~~(2011)~~.

329 The prognostic variables (e.g., SWE) in the LSM are determined by meteorological forcing
330 variables such as 2-m air temperature, humidity, 10-m wind speed, precipitation, surface
331 pressure, and radiative fluxes. The 3-hourly, JRA55 reanalysis at 0.56° spatial resolution is
332 employed for the meteorological forcing variables, which is linearly interpolated to a 50 km
333 resolution of the LSM. The model background error needed for data assimilation is estimated
334 by JULES ensemble runs with perturbed initial and boundary conditions. Following the
335 previous studies (Reichle et al., 2008; Seo et al., 2021), meteorological forcing variables are
336 perturbed ~~due to randomness~~ to account for the uncertainties in these variables, especially
337 precipitation, downward shortwave, and downward longwave. Perturbations are applied using
338 additive adjustments assuming a normal distribution for longwave radiation and multiplicative
339 adjustments following a log-normal distribution for shortwave radiation and precipitation, as
340 guided by previous studies (Seo et al., 2021). Here, the ensemble means of additional and
341 multiplicative perturbations are zero and one, respectively. The relationship between disturbed
342 precipitation and radiative flux ensures the physical consistency among atmospheric forcing
343 variables (Reichle et al., 2008). For instance, a negative anomaly in precipitation and

344 downward longwave-radiation is statistically linked to a positive anomaly of downward
345 shortwave-radiation. Detailed explanations regarding the perturbation of atmospheric forcings
346 can be found in Reichle et al. (2008).

347

348 3. Methodology

349 3.1. Bias correction

350 The ~~discrepancies~~discrepancy in SWE between remote sensing and LSMs ~~are~~ often ~~caused by~~
351 ~~arises due to~~ uncertainties in the model physics and ~~meteorological~~-forcing data- ~~and satellite~~
352 ~~retrievals~~. These ~~differences~~uncertainties can lead to ~~a~~ significant ~~biases in the variance and~~
353 ~~mean of~~discrepancy in SWE between model simulations and satellite remote-sensing retrievals,
354 ~~and such biases can result in poor~~potentially degrading performance. In previous studies (e.g.,
355 Reichle and Koster, 2004; Seo et al., 2021), a scaling method of the nonlinear cumulative
356 distribution function (CDF) matching is used to account for the systematic bias of soil moisture
357 in the model backgrounds. However, ~~unlike soil moisture, SWE presents varying~~
358 ~~characteristics in this study, it is difficult to apply it as~~ the CDF distribution ~~across different~~
359 ~~regions, such as between high and low latitudes, thus requiring the estimation of SWE could~~
360 ~~not be clearly simulated due to~~ distribution at each grid point. ~~As a result,~~ the insufficient sample
361 size ~~hinders the clear simulation of the CDF distribution, posing challenges in its application~~.
362 To address this issue, we attempted to apply a simple and effective standard normal deviation
363 scaling to satellite-derived SWE, ~~considering its potential use as initial conditions for JULES~~
364 ~~LSM-based climate models~~. Based on the climatology and standard deviation for the model
365 and remote sensing retrievals, the scaled SWE (O_{new}) from the satellite can be derived from
366 the following relation:

367

$$368 \quad O_{new} = \left(\frac{O - \bar{O}}{\sigma_o} \times \sigma_m \right) + \bar{M} \quad (1)$$

369

370 ~~,~~ where $\bar{O}(\sigma_o)$ and $\bar{M}(\sigma_m)$ indicate climatology (standard deviation) of remote sensing
371 retrievals and the model, respectively. This approach has been widely utilized in observation-

372 based land initialization and has proven to be effective (e.g., Koster et al., 2011; Jeong et al.,
373 2013).

374

375

3.2. SnowData assimilation method

The snow assimilation is conducted based on the LETKF (e.g., Hunt et al., 2007), which is utilized to combine ~~satellite remote sensing~~remotely sensed retrievals with the LSM model outputs (a.k.a. backgrounds) to produce a snow analysis. ~~LETKF is a powerful~~Unlike variational data assimilation ~~method and methods, non-variational approaches (i.e., ensemble-based filters)~~ characterize a probabilistic representation with the spread of the ensemble serving as an estimate of forecast uncertainty. LETKF has several advantages over other data assimilation methods. First, LETKF can efficiently handle large datasets and high-dimensional state variables by localizing the covariance matrix. This offers efficiency in parallel computing, making it suitable for real-time forecasting and high-resolution data assimilation. ~~Secondly~~In this study, the ~~method utilizes model simulation ensembles to capture the uncertainty in the initial states~~horizontal local patch size and ~~model errors, which allows for a better representation of the true probability distribution of the state variables that vary in time~~the localization length scale parameters are defined as 150 km and space. ~~Third, LETKF applies an adaptive inflation scheme, which adjusts the ensemble spread to account for the observational and model errors, ensuring that the uncertainty estimates are realistic and not underestimated nor overestimated. In LETKF, the analysis states~~ (X^a) are obtained by

$$X^a = \bar{X}^a + \delta X^a \quad (2)$$

~~, where \bar{X}^a and δX^a are the matrices of analysis ensemble means and perturbations,~~30 km (Table 1), respectively. ~~They are defined by~~

$$\bar{X}^a = \bar{X}^f + \delta \tilde{x}^a \quad (3)$$

$$\delta X^a = \delta X^f [(K - 1) \tilde{P}^a]^{1/2}. \quad (4)$$

~~Here, the analysis ensemble means~~ (\bar{X}^a) is determined by gathering the analysis increment $(\delta \tilde{x}^a)$ to the model ensemble mean (\bar{X}^f) produced by the JULES land surface model. The analysis ensemble perturbation (δX^a) is computed considering the model perturbation (δX^f) , the

number of model ensembles (K), and the analysis error covariance (\tilde{P}^a) in the ensemble space. The analysis increment ($\delta\tilde{x}^a$) is acquired by considering the difference between the SWE of AMSR2 used as observation and the model ensembles produced by the JULES LSM and determined by

$$\delta\tilde{x}^a = \delta X^f \tilde{P}^a \delta Y^T R^{-1} (y^o - \overline{H(X^f)}), \text{ and} \quad (5)$$

$$\tilde{P}^a = \left[\frac{(K-1)t}{\rho} + \delta Y^T R^{-1} \delta Y \right]^{-1}. \quad (6)$$

It consists of the model ensemble perturbation (δX^f), the analysis error covariance (\tilde{P}^a), observation error covariance (R), model ensemble perturbation in the observation grid (δY), and observation innovation ($y^o - \overline{H(X^f)}$) derived from the difference between the model ensemble in the observation grid ($\overline{H(X^f)}$) and the observation (y^o). Here, H represents the observation operator, projecting the modeled snow background onto the satellite observation locations using bilinear interpolation. ρ denotes the covariance inflation factor for the \tilde{P}^a , aiding in preventing underestimation of the covariance. This study applies multiplication-based 20% inflation (ρ) for the ensemble spread derived from 24 member ensembles. Therefore, the final analysis state (X^a) is written as

$$X^a = \bar{X}^f + \delta X^f \left[\tilde{P}^a \delta Y^T R^{-1} (y^o - \overline{H(X^f)}) + [(K-1)\tilde{P}^a]^{-\frac{1}{2}} \right]. \quad (7)$$

This approach involves the weight function ($w(d_r)$) for the covariance localization within the local patch centered at the analysis grid (e.g., Houtekamer and Mitchell, 2001; Hamill et al., 2001). This function assigns larger errors to observations located farther away from the center of the local patch, as proposed by Miyoshi and Yamane (2007), depending on the Gaussian function as (2007), depending on the Gaussian function. Secondly, the method utilizes model simulation ensembles to capture the uncertainty in the initial states and background errors, which allows for a better representation of the flow-dependent probability distribution of the state variables that vary in time and space. Third, the LETKF employs an

425 inflation parameter to adjust the ensemble spread, ensuring realistic uncertainty estimation by
426 accounting for background errors. The underestimation of the analysis error covariance is
427 typically issued by spatially and temporally constant boundary conditions and observation
428 errors and limited ensemble members. Based on the standardized LETKF, this study applies a
429 multiplicative covariance inflation of 20% of the spread of 24 member ensembles for each data
430 assimilation cycle. Furthermore, the Kalman gain analysis (Seo et al., 2021), which quantifies
431 the ratio of the background error to the total error (equivalent to the sum of the background and
432 the observation error), is conducted. This analysis serves to determine the weights assigned to
433 assimilated observations in the analysis update processes of the LETKF.

$$434 \quad w(d_j) = \frac{e^{-\frac{d_j^2}{\sigma^2}}}{\sum_j e^{-\frac{d_j^2}{\sigma^2}}} \quad (8)$$

435 ~~—where σ denotes a parameter of the localization length scale and d_j indicates the distance of~~
436 ~~j -th observed value from the center of each local patch. In this study, the horizontal local patch~~
437 ~~size and the localization length scale parameters are defined as 150 km and 30 km (Table 1),~~
438 ~~respectively. Detailed information about the LETKF algorithm and its implementation can be~~
439 ~~referenced in Hunt et al. (2007) and Shlyueva et al. (2013).~~

441 **3.3. Snow data assimilation design**

442 This study conducts the advanced snow data assimilation experiment at a daily cycle based
443 on LETKF with the satellite data and the JULES LSM model outputs driven by 3-hourly JRA55
444 reanalysis atmospheric forcing. The snow assimilation processes are illustrated in Fig. 1, with
445 a more detailed description in Table 1. Since data assimilation is conducted by considering the
446 error of SWE in both the model and the observation, it is important to accurately understand
447 the observation and modelbackground errors to improve the performance of data assimilation.
448 The experiment calculates the modelbackground error from the 24 ensemble member spreads

449 generated by perturbing atmospheric forcings such as longwave radiation, shortwave radiation,
450 and precipitation in JULES LSM, as provided in section 2.3. ~~The~~Due to the absence of precise
451 error estimates for AMSR2 SWE retrievals, the observation error is conservatively prescribed
452 as 10% of AMSR2 SWE for each grid compared to the previous study utilizing AMSR2 SWE
453 data (Lee et al., 2015), ~~because it usually increases~~considering the general increase in the errors
454 during the snow accumulation period with the ~~developing~~development of deep snowpack
455 (Foster et al., 2005; Cho et al., 2017). Here, the bias-corrected AMSR2 satellite data as
456 described in section 3.1 is used as the observation data, and the updated snow analysis state (~~X^e~~)
457 through data assimilation becomes a new initial state for the next integration in JULES LSM
458 (Fig. 1). In addition, the analysis state of this method is calculated based on the IMS snow
459 cover fraction as a reference in the following way (Fig. 1); where the SCF of IMS is zero, the
460 snow amount analysis is set to zero, and in other cases, it is derived from data assimilation. The
461 reason for this is due to the importance of the presence or absence of snow in the climate system,
462 as well as the high reliability of the IMS data. (e.g., Brown et al., 2014). A background
463 experiment of JULES LSM without satellite data assimilation as a baseline (referred to
464 hereafter as “Openloop”) is also achieved by employing the same ensemble perturbations,
465 thereby measuring the skill improvement from the snow analysis state through the assimilation
466 of satellite-derived SWE and IMS SCF from satellite and surface observations (referred to
467 hereafter as “DA”). All experiments are conducted in April from 2013 to 2020, which is one
468 of the months with low snow performance in the LSM when the snow begins to melt in the
469 Northern Hemisphere (e.g., Toure et al., 2018; You et al., 2020).

470 4. Results

471 4.1. Skill Verification

472 Figure 2 displays the climatological-mean SCF from the IMS multi-satellite data (Brown
473 et al., 2014) and the differences from AMSR2, Openloop, JRA55, and DA for April 2013-2020.
474 Here, the JRA55 SWE serves as a reference dataset for comparison with other reanalyses and
475 is associated with meteorological forcing data used in the JULES land surface model. April is
476 a season when the accumulated snow during the cold season begins to melt. This study defines
477 the transitional region with a climatological-mean SWE of less than 16 mm as in previous
478 studies (e.g., Gan et al., 2021), the boundary of these transition regions is represented by the
479 black lines in Fig. 2. The transitional regions exhibit large variability in space and time, and
480 they are mainly located at mid-latitudes. The SCF climatology patterns show negligible
481 differences in high latitudes of heavy snow accumulation but noticeable differences in the
482 transitional mid-latitude regions of less snow. SCF from JRA55 tends to be underestimated
483 compared to IMS, whereas AMSR2 and Openloop tend to overestimate. There is a clear
484 difference in SCF between AMSR2 and IMS satellite data. This study gives more credibility
485 to IMS than AMSR2, as the former is based on multiple satellite data sources (e.g., Brown et
486 al., 2014). As we used the IMS SCF to define the snow region to be assimilated by AMSR2
487 SWE, it is natural that DA shows better consistency with IMS and reduces overestimation
488 biases in Openloop. Quantitatively, the root mean square differences (accuracy, defined in
489 supplementary Table 1 as in previous study) for AMSR2, Openloop, JRA55, and DA with
490 (from) IMS are 0.23 (0.91), 0.18 (0.91), 0.13 (0.93), and 0.13 (0.97), respectively, showing the
491 best consistency in DA. The quantitative differences between DA and other experimental
492 results are minor, but noticeable spatial discrepancies exist, particularly around transition
493 regions.

494 The SWE climatology from AMSR2, Openloop, JRA55, and DA is also compared with

495 CMC as a reference in Fig. 3. The SWE derived from AMSR2 shows a significant
496 underestimation compared to CMC, particularly in the regions with heavy snow accumulation
497 at high latitudes. This is presumed to be due to limitations in satellite sensors detecting the
498 depth of snow (~~Gan et al., 2021~~). (Gan et al., 2021). The SWE from JRA55 exhibits
499 characteristics of overestimation in high latitudes and underestimation in transitional regions.
500 On the other hand, the climatological SWEs from Openloop and DA exhibit higher
501 correspondence to CMC, even higher than JRA55. Specifically, DA demonstrates a higher
502 agreement with CMC, despite the marginal difference compared to Openloop. Quantitatively,
503 the pattern correlation coefficients (root mean square differences) for AMSR2, Openloop,
504 JRA55, and DA with (from) CMC are 0.63 (80.7 kg/m²), 0.80 (50.1 kg/m²), 0.60 (100.8 kg/m²),
505 and 0.80 (49.9 kg/m²), respectively. Due to the application of standard deviation scaling to the
506 satellite-derived SWE used in data assimilation, the discrepancy in climatological SWE
507 distributions between DA and Openloop is deemed negligible. Despite its similarity to
508 Openloop, DA with snow data assimilation displays the relatively highest correlation and the
509 smallest root mean square difference among the datasets, indicating the benefit of assimilating
510 the AMSR2 SWE despite the relatively lower performance of the satellite data itself.

511 Next, we compare the temporal variation of SWE as measured by the Spearman rank
512 correlation coefficient with CMC, which is regarded as more appropriate than the Pearson
513 correlation coefficient for describing ~~nonlinear variables~~ datasets containing nonlinearity and
514 outliers such as snow in both time and space. Figure 4 compares the distribution of correlation
515 skills from AMSR2, Openloop, JRA55, and DA. Openloop has a high performance in regions
516 with heavy snow accumulation but relatively low performance in transition regions with
517 significant snow changes. In contrast, the results from the AMSR2 satellite data represent poor
518 performance in high-latitude areas with heavy snow accumulation but high performance in
519 transitional regions, consistent with the previous studies (Gan et al., 2021). DA shows high

520 performance not only in high-latitude areas with heavy snow accumulation but also in transition
521 regions. Even compared to JRA55 used as the atmospheric forcing, DA performs better in
522 temporal variation. The quantitative results in the correlation in the Northern Hemisphere over
523 40°N (the transition region) are 0.41 (0.54) for AMSR2, 0.61 (0.48) for Openloop, 0.58 (0.58)
524 for JRA55, and 0.67 (0.61) for DA, respectively. The findings indicate that satellite retrievals
525 offer additional value in capturing temporal variations through data assimilation, indicating
526 the benefit of assimilating the AMSR2 SWE despite the overall lower performance of the
527 satellite data itself.

528 The performance improvement by DA is also evident in the zonally-averaged correlation
529 coefficient shown in Fig. 5. The AMSR2 satellite data shows higher performance than
530 Openloop in the transition region around latitude 45 °N-55 °N, although performance sharply
531 decreases with increasing snow accumulation. Openloop indicates gradually increasing
532 performance as the latitude increases, with the highest performance at around 60°N. DA
533 denotes superior performance across the Northern Hemisphere, especially in the mid-latitude
534 transition region than AMSR2 or JRA55. An exception is for 35-40°N in the Tibetan Plateau,
535 where JRA55 used in-situ observations. The results suggest that the developed snow data
536 assimilation system represents well not only the transitional regions but also the satellite-
537 limited regions with heavy snow.

538 Figure 6 presents the Spearman rank correlation depending on the SWE amount in the
539 Northern Hemisphere. AMSR2 exhibits higher performance than Openloop for SWE up to 16
540 mm. However, the performance of AMSR2 sharply declines beyond that threshold, and
541 Openloop shows a better performance. Consistent with the results illustrated in Figs. 4 and 5,
542 DA demonstrates superior performance compared to others. Note that DA performs
543 significantly better in the transition region of less than 16 mm of SWE. Considering that the
544 area below 16 mm of SWE accounts for approximately 53% of the entire area of the Northern

545 Hemisphere(as shown in the pie chart in Fig. 6), the data assimilation impact is identifiable,
546 and it can contribute substantially to the increase in the prediction skill through improving the
547 simulation of the albedo changes and surface energy balance.

548 ~~This~~Consistent with the description in Section 3.3, this study ~~conducted~~considers an
549 algorithm based on the highly reliable IMS satellite SCF data to identify the presence of snow
550 and determine the assimilation process. Therefore, a further sensitivity test is conducted to
551 investigate the influence of incorporating IMS ~~snow cover data~~ in snow assimilation. Figure 7
552 compares the correlation differences between Openloop and the data assimilation result
553 employing both AMSR2 and IMS_(DA), as well as the data assimilation result utilizing solely
554 AMSR2 and excluding IMS_(hereafter referred to as DA_AMSR2). The results obtained from
555 the snow assimilation show the improvements in the transitional regions where AMSR2
556 denotes a better agreement with the observations compared to Openloop. Notably, the skill is
557 enhanced significantly in DA by incorporating the IMS SCF. ~~There are exceptional areas where~~
558 DA ~~performsexhibits~~ inferior performance compared to Openloop in certain exceptional cases,
559 which ~~are associated with the differences in SCF~~may be attributed to discrepancies in snow
560 identification between the CMC observations used for correlation and the IMS and CMC data
561 utilized for data assimilation. Moreover, the performance of SWE improves even when only
562 AMSR2 is used, but incorporating IMS leads to a substantial improvement in the transitional
563 regions. This implies that IMS has a positive influence on the snow data assimilation.

564

565

566 **4.2 Kalman gain analysis**

567 In order to better understand the skill enhancement through snow assimilation of satellite
568 data, this section examines the Kalman gain, ~~which represents the weights of the assimilated~~
569 ~~observations in the analysis update of LETKF.~~ Figure 8 illustrates the spatial distribution of

570 observation error, model background error, and the Kalman gain. A high value of the Kalman
571 gain denotes that the assimilated result is closer to the AMSR2 observation than the model
572 background. The Kalman gain is large when the model background error becomes large, or the
573 observation error is small. As this study specifies the observation error as a conservative 10%
574 of SWE compared to the previous study (Lee et al., 2015), the observation error basically
575 follows the distribution similar to the climatological-mean values. The background errors,
576 originating from the 24 ensemble members, have higher values in high-latitude regions and
577 mid-latitude regions. Data assimilation methods such as LETKF used in this study often face
578 challenges in accurately representing background errors when the ensemble spread is
579 insufficient. Generally, the magnitude of ensemble spread is frequently compared to the root
580 mean square error (RMSE). The background error ensemble spread in this study demonstrates
581 a sufficiently valid magnitude in comparison with the RMSE, as illustrated in SFig. 1,
582 indicating that it is well estimated. Moreover, the SWE distribution among ensemble members
583 consistently exhibited a Gaussian distribution, with a distinct this distribution particularly
584 evident in transitional regions (SFig. 4). In the spatial distribution of Kalman gain in Fig. 8c,
585 significant performance improvement is observed in transition regions, where Kalman gains
586 exhibit larger values. However, in high-latitude areas with substantial snow accumulation, there
587 is a tendency for Kalman gain to have lower values. These findings agree well with the bar
588 graph in Fig. 9, which illustrates the Kalman gain as a function of SWE amount. In the region
589 encompassing the transition region with SWE amounts below 20 mm, the Kalman gain displays
590 the highest values, particularly exceeding 0.8. As the SWE amount increases, the Kalman gain
591 decreases, with a significant decline observed when the SWE amount reaches 80-100 mm or
592 higher. Furthermore, in the areas where DA denotes improved skill compared to Openloop, the
593 Kalman gain shows values generally above 0.7. In contrast, relatively lower values below 0.5
594 are observed in the areas with decreased skill. This indicates that in the dominant areas of

595 performance improvement, including the transition region, the background error is
596 significantly larger than the observation error, emphasizing the substantial influence of
597 observations in data assimilation. It is found that accurate remote sensing retrievals are well
598 reflected in regions with high uncertainty in the LSM through the snow data assimilation
599 system, leading to performance improvement.

600

601

602 **4.3 Validation of the SWE for the extreme event**

603 In April 2020, Siberia experienced a record-breaking heatwave with the highest observed
604 average temperature. This section investigates the potential benefits of snow assimilation using
605 satellite data for the case of the 2020 Siberian heatwave. Previous studies have identified the
606 strong polar vortex accompanied by the AO amplification during winter as a major cause of
607 the cold Eurasian region (Overland and Wang, 2021). Additionally, it has been revealed that
608 the occurrence of high temperatures in the Siberian region is found to be closely ~~related to the~~
609 ~~development of~~associated with large-scale atmospheric waves in the upper atmosphere ~~of~~over
610 the Eurasian region, ~~indicating a significant influence on the strengthened land-atmosphere~~
611 ~~interaction in recent years. originating from the Atlantic (De Angelis et al., 2023).~~ As a result,
612 remarkable snow melting occurred due to the high surface temperature over the Siberian region
613 in April 2020, leading to extremely low values of SWE and SCF as depicted in SFig. 2. This is
614 consistent with previous studies reporting a significant snow depletion in 2020 in the region
615 (Gloege et al., 2022). Especially, as shown in Fig. 10, significant negative anomalies in SWE
616 and SCF are predominant over the transition region. ~~With a substantial~~Substantial snow ~~melting,~~
617 ~~it increases the~~melt can contribute to record-breaking heatwaves through albedo feedback and
618 changes in the ratio of the latent and sensible heat ~~flux to the atmosphere, thereby~~
619 strengthening fluxes from the ~~upper-level waves by enhanced atmosphere-land interaction,~~

620 ~~leading~~exposed surface, coupled with favorable atmospheric circulation patterns (Collow et al.,
621 2022). Collow et al. (2022) demonstrated that the exposed surface contributed to ~~further~~
622 ~~intensification of heatwaves~~.up to 20% of the temperature anomaly over Siberia in spring 2020.
623 This implies the importance of realistic snow initial states in the global coupled model forecasts.
624 For the Siberian region with extreme high-temperature events marked by the red box in Fig.
625 10, DA shows a better agreement with the extremely dry snow conditions, especially in the
626 transitional region, compared to the Openloop. These results are evident when considering the
627 observation-to-model ratio in that region. The percentage of CMC_(IMS) is ~~83%~~(78%) for
628 Openloop and ~~93%~~(89%) for DA, indicating that DA with snow data assimilation based on
629 satellite data ~~produces more significant changes~~ineffectively replicates the observed snow
630 depletion in comparison with Openloop. Similarly to the 2020 case, we obtained another
631 significant case in 2014 compared to Openloop, as shown in SFig. 3. Such extremely dry snow
632 conditions can provide significant heatwave events in the following months.

633
634
635
636
637
638

639 **5. Conclusions and discussion**

640 The advanced ~~snow~~SWE data assimilation is developed in this study with the LETKF data
641 assimilation method ~~based on~~and the JULES LSM. The system assimilates snow water
642 equivalent retrievals from AMSR2 and IMS snow cover. This constitutes an objective way to
643 optimally combine two imperfect data sources for SWE from satellite remote sensing
644 observations data and the land surface model simulation forced by observed atmospheric data.
645 This study ~~showed~~shows that the satellite-derived ~~snow data~~SWE has limitations in penetrating
646 deep snow, and exhibited much discrepancy from the ~~snow~~SWE obtained from the Openloop
647 LSM simulations. The ~~snow~~SWE assimilation ~~framework developed~~ in this study proves the
648 beneficial impacts of using satellite snow data, maintaining better analysis quality ~~both in the~~
649 ~~regions with low satellite data quality and the high satellite data quality~~ by dynamically
650 balancing the errors from the satellite observations and the model background ~~forecasts. states.~~

651 It is found that the simulation from Openloop as a baseline shows superior performance in
652 high-latitude regions with heavy snow accumulation but relatively inferior performance in
653 transition regions with ~~significant~~ much variation of snow ~~changes in space and time.~~
654 Contrastingly, the ~~results of the~~ AMSR2 satellite data represent poor performance in high-
655 latitude regions but exhibit ~~good performance in transition regions. AMSR2 demonstrates~~
656 ~~higher performance than Openloop up to 16 mm of SWE, but beyond that threshold, the skill~~
657 ~~of AMSR2 sharply declines while Openloop shows~~relatively better performance. ~~DA with~~
658 ~~snow~~ in the transition regions. The SWE from the LETKF data assimilation consistently
659 ~~performs~~exhibits better performance in capturing the ~~climatological mean pattern~~climatology
660 and temporal variation compared to other results. ~~Notably, It specifically improves the snow~~
661 ~~assimilation system in this study reflects well~~analysis in the ~~errors and advantages of land~~
662 ~~surface models and satellite derived data, controlling not only the~~ mid-latitude transition
663 regions ~~but also the satellite limited~~ that cover approximately 53% of the entire areas of the

664 Northern Hemisphere. It is found that the model background errors estimated from the
665 ensemble spread are significantly larger than the observation errors, thereby reflecting satellite
666 information more in those regions with. The LETKF data assimilation also proves reliable
667 representation in the heavy snow regions due to low ensemble spread and large uncertainty in
668 the satellite retrievals. Moreover, during the record-breaking heatwave in Siberia in April 2020,
669 the remarkable snow depletion observed due to high surface temperatures is more realistically
670 reproduced by our snow analysis compared to the Openloop.

671 ~~The significant improvement of SWE data assimilation is primarily observed in the~~
672 ~~transition regions of less than 16 mm, which accounts for approximately 53% of the entire~~
673 ~~areas of the Northern Hemisphere. A sensitivity test also revealed that the use of IMS SCF led~~
674 ~~to a substantial improvement in the transitional regions, in addition to the use of AMSR2 SWE.~~
675 ~~The sources contributing to the skill improvement of SWE in the snow assimilation system can~~
676 ~~be explained through Kalman gain analysis, measuring the relative importance of observations~~
677 ~~given the model background errors. Higher Kalman gains values above 0.7 were observed in~~
678 ~~the transition regions, whereas they decreased below 0.5 in the high latitudes with heavy snow~~
679 ~~accumulation. It found that in the dominant areas of performance improvement, including the~~
680 ~~transition region, the background error is significantly larger than the observation error,~~
681 ~~emphasizing the substantial influence of observations in the snow assimilation process.~~

682 ~~In the case of the Siberian heatwave, remarkable snow melting occurred due to high surface~~
683 ~~temperature over the Siberian region in April 2020. It resulted in extremely low values of SWE~~
684 ~~and SCF, leading to a further intensification of the heatwave. The SWE anomalies from the~~
685 ~~snow data assimilation with the AMSR2 satellite showed significant changes in snow that~~
686 ~~seemed to better explain the heatwave episode than the Openloop.~~This snow data assimilation
687 framework is anticipated to contribute to a more precise prediction of atmospheric conditions
688 by realistically capturing the interaction between the atmosphere and land, given the substantial

689 influence of SWE on energy and water balance at the interface of the atmosphere and land.
690 Specifically, this applies to the transitional regions with high spatial and temporal variability.
691 The long-term analysis of snow manifests a pronounced variability in the continental interior
692 at the interannual timescales, potentially improving the prediction of extreme heatwave events
693 by global climate models. This study used the gridded CMC data from in-situ observations for
694 the validation. Although existing snow data are subject to much uncertainty and limitations, we
695 expect to obtain comparable conclusions and significant benefits of optimally combining
696 satellite SWE data and the LSM model simulations through LETKF data assimilation method.

697 The quality of the observation is crucial in the data assimilation system. Satellite-derived
698 snow cover exhibits a significantly higher accuracy compared to other data sources, while SWE
699 has restricted performance due to the limitations of penetration depth by satellite sensors and
700 relies heavily on estimation algorithms. Due to these problems, most previous studies and
701 operational centers primarily depend on satellite-derived snow cover for snow initialization.
702 However, the findings from this study highlighted the beneficial impacts of using satellite-
703 derived SWE, particularly in the rapidly changing transition areas, to find out which variable
704 is more important in closing surface energy and water balance changed by snow. Nevertheless,
705 areas of significance in large-scale circulation, such as the Tibetan region, which experiences
706 significant uncertainty and degraded performance in satellite data, do not exhibit substantial
707 data assimilation effects. As the performance of SWE derived from various satellites continues
708 to advance, these issues will be discussed more. _

709 ~~Improved snow estimates from the snow assimilation system can enhance the initialization~~
710 ~~of climate models used in most of the seasonal forecast operation centers. As snow significantly~~
711 ~~influences energy and water balance at the atmosphere-land boundary, this approach allows for~~
712 ~~a more accurate prediction of atmospheric conditions by realistically representing atmosphere-~~
713 ~~land interactions. Specifically, this applies to transitional regions where the reliability of snow~~

714 ~~estimation performance through model simulations is compromised. The long-term analysis of~~
715 ~~snow manifests a pronounced variability in the continental interior at the interannual timescales,~~
716 ~~potentially improving the prediction of extreme heatwave events by global couple models. This~~
717 ~~study used the gridded CMC data as a validation reference, which is based on in-situ~~
718 ~~observations. Despite much uncertainty and limitations of this dataset, we expect to obtain~~
719 ~~comparable conclusions to this study through comparisons with other independent,~~
720 ~~observation-based datasets.~~

721

722

723 **Key words**

724 Snow data assimilation, AMSR2, LETKF, snow water equivalent, JULES LSM

725

726 ***Data availability.***

727 The AMSR2 SWE and IMS SC were obtained from

728 https://n5eil01u.ecs.nsidc.org/AMSA/AU_DySno.001/ and

729 <https://noadata.apps.nsidc.org/NOAA/G02156/>, respectively. The CMC SWE was collected

730 from https://daacdata.apps.nsidc.org/pub/DATASETS/nsidc0447_CMC_snow_depth_v01/.

731 The snow-assimilated results and land surface variables from the LSM offline simulation may

732 be requested from the authors.

733

734 ***Author contributions.***

735 LJI conceived the project, designed the study, developed the snow assimilation system, wrote

736 the paper, and made the figures. LMI provided advice on the methods, project design, and

737 review and editing of the manuscript. TSL helped with the experiment with the land surface

738 model. SEK helped with the data assimilation method based on LETKF. LYK provided advice

739 on snow satellite data and the sensitivity methods. All authors contributed to the writing of the

740 paper by providing comments and feedback.

741

742 ***Competing interests.***

743 The contact author has declared that none of the authors has any competing interests.

744

745 *Acknowledgements*

746 This work was funded by the Korea Meteorological Administration Research and Development
747 Program under Grant KMI2021-01210. ES was supported by Learning & Academic research
748 institution for Master's·PhD students, and Postdocs (LAMP) Program of the National Research
749 Foundation of Korea (NRF) grant funded by the Ministry of Education (RS-2023-000301702).

750

751

752

753 **Reference**

- 754 Allen, R.J., Zender, C.S.: Forcing of the Arctic Oscillation by Eurasian snow cover. *J. Clim.* 24 (24),
755 6528-6539, 2011.
- 756 Best, M.J., Pryor, M., Clark, D.B., Rooney, G.G., Essery, R., Ménard, C.B., Edwards, J.M., Hendry, M.A.,
757 Porson, A., Gedney, N., Mercado, L.M., Sitch, S., Blyth, E., Boucher, O., Cox, P.M.,
758 Grimmond, C.S.B., Harding, R.J.: The Joint UK Land Environment Simulator (JULES), model
759 description–Part 1: energy and water fluxes. *Geosci. Model Dev.* 4, 677–699, 2011.
- 760 Boone, A., Habets, F., Noilhan, J., Clark, D., Dirmeyer, P., Fox, S., Gusev, Y., Haddeland, I., Koster, R.,
761 Lohmann, D., Mahanama, S., Mitchell, K., Nasonova, O., Niu, G.Y., Pitman, A., Polcher, J.,
762 Shmakin, A., Tanaka, K., van den Hurk, B., Verant, S., Verseghy, D., Viterbo, P., Yang, Z.L.: The
763 Rhone-Aggregation land surface scheme intercomparison project: an overview. *J. Clim.* 17,
764 187–208, 2004.
- 765 Brasnett, B.: A global analysis of snow depth for numerical weather prediction. *J. Appl. Meteorol.* 38
766 (6), 726–740, 1999.
- 767 Brown, L.C., Howell, S.E., Mortin, J., Derksen, C.: Evaluation of the Interactive Multisensor Snow and
768 Ice Mapping System (IMS) for monitoring sea ice phenology. *Remote Sens. Environ.* 147,
769 65–78. doi: 10.1016/j.rse.2014.02.012, 2014.
- 770 Brown, R.D., Brasnett, B.: Canadian Meteorological Centre (CMC) Daily Snow Depth Analysis Data.
771 NASA National Snow and Ice Data Center Distributed Active Archive Center, Boulder,
772 Colorado, USA. <https://doi.org/10.5067/W9FOYWH0EQZ3>, 2010.
- 773 Brown, R.D., Brasnett, B., Robinson, D.: Gridded North American monthly snow depth and snow
774 water equivalent for GCM evaluation. *Atmos.–Ocean*, 41, 1–14, 2003.
- 775 Broxton, P.D., Zeng, X., Dawson, N.: The impact of a low bias in snow water equivalent initialization
776 on CFS seasonal forecasts. *J. Clim.* 30 (21), 8657–8671. [https://doi.org/10.1175/JCLI-D-17-](https://doi.org/10.1175/JCLI-D-17-0072.1)
777 [0072.1](https://doi.org/10.1175/JCLI-D-17-0072.1), 2017.
- 778 Brubaker, K., Pinker, R., Deviatova, E.: Evaluation and comparison of MODIS and IMS snow-cover
779 estimates for the continental United States using station data. *J. Hydrometeorol.* 6, 1002–
780 1017, 2009.
- 781 [Burke, E. J., Dankers, R., Jones, C. D., and Wiltshire, A. J.: A retrospective analysis of pan Arctic](#)
782 [permafrost using the JULES land surface model, *Clim. Dynam.*, 41, 1025–](#)
783 [1038, <https://doi.org/10.1007/s00382-012-1648-x>, 2013.](#)
- 784 Chen, M., Wang, W., Kumar, A.: Prediction of monthly-mean temperature: The roles of atmospheric
785 and land initial conditions and sea surface temperature *J. Clim.* 23(3), 717-725, 2010.
- 786 Cho, E., Tuttle, S.E., Jacobs, J.M.: Evaluating consistency of snow water equivalent retrievals from
787 passive microwave sensors over the north central US: SSM/I vs. SSMIS and AMSR-E vs.
788 AMSR2. *Remote Sens.* 9(5), 465, 2017.
- 789 Cohen, J., Barlow, M., Kushner, P. J., Saito, K.: Stratosphere–troposphere coupling and links with
790 eurasian land surface variability. *J. Clim.* 20(21), 5335–5343.
791 <https://doi.org/10.1175/2007jcli1725.1>, 2007.

792 [Collow, A.B.M., Thomas, N.P., Bosilovich, M.G., Lim, Y.K., Schubert, S.D., Koster, R.D.: Seasonal variability](#)
793 [in the mechanisms behind the 2020 Siberian heatwaves. J. Clim. 35\(10\), 3075-3090, 2022.](#)

794 Dawson, N., Broxton, P., Zeng, X.: Evaluation of remotely sensed snow water equivalent and snow
795 cover extent over the contiguous United States. J. Hydrometeorol. 19 (11), 1777–1791.
796 <https://doi.org/10.1175/JHM-D-18-0007.1>, 2018.

797 [De Angelis, A.M., Schubert, S.D., Chang, Y., Lim, Y.K., Koster, R.D., Wang, H., Marquardt Collow, A.B.:](#)
798 [Dynamical Drivers of the Exceptional Warmth over Siberia during the Spring of 2020. J.](#)
799 [Clim. 36\(15\), 4837-4861, 2023.](#)

800 De Lannoy, G.J.M., Reichle, R.H., Houser, P.R., Arsenault, K.R., Verhoest, N.E.C., Pauwels, V.R.N.: Satellite-
801 scale snow water equivalent assimilation into a high-resolution land surface model. J.
802 Hydrometeorol. 11 (2), 352–369. <https://doi.org/10.1175/2009JHM1192.1>, 2010.

803 De Rosnay, P., Balsamo, G., Albergel, C., Muñoz-Sabater, J., Isaksen, L. Initialisation of land surface
804 variables for numerical weather prediction. Surv. Geophys. 35, 607-621, 2014.

805 Dee, D., Uppala, S., Simmons, A., Berrisford, P., Poli, P., Kobayashi, S., Andrae, U., Balsameda, M.,
806 Balsamo, G., Bauer, P., Bechtold, P., Beljaars, A.C.M., van de Berg, L., Bidlot, J., Bormann, N.,
807 Delsol, C., Dragani, R., Fuentes, M., Geer, A.J., Haimberger, L., Healy, S.B., Hersbach, H., Hólm,
808 E.V., Isaksen, L., Kållberg, P., Köhler, M., Matricardi, M., McNally, A.P., Monge-Sanz, B.M.,
809 Morcrette, J.-J., Park, B.-K., Peubey, C., de Rosnay, P., Tavolato, C., Thépaut, J.-N., Vitart, F.: The
810 ERA-Interim reanalysis: Configuration and performance of the data assimilation system. Q.
811 J. R. Meteorol. Soc. 137, 553–597, 2011.

812 [Dirmeyer, P., Derome J, Lin H, Brunet, G.: Seasonal forecasting with a simple general circulation model:](#)
813 [Predictive skill in the AO and PNA. J. Clim., 15, 597–609, 2005.](#)

814 [Dirmeyer, P.A.: The terrestrial segment of soil moisture–climate coupling. Geophys. Res. Lett. 38\(16\),](#)
815 [2011.](#)

816 [Dirmeyer, P.A., Gao, X., Zhao, M., Guo, Z., Oki, T., Hanasaki, N.: The Second Global Soil Wetness](#)
817 [Project \(GSWP-2\): Multi-model analysis and implications for our perception of the land](#)
818 [surface. Bull. Amer. Meteor. Soc. 87, 1381–1397, 2006.](#)

819 Dutra, E., Schär, C., Viterbo, P., Miranda, P. M.: Land-atmosphere coupling associated with snow
820 cover. Geophys. Res. Lett. 38 (15) , 2011.

821 Dziubanski, D.J., Franz, K.J.: Assimilation of AMSR-E snow water equivalent data in a spatially-lumped
822 snow model. J. Hydrol. 540, 26–39. <https://doi.org/10.1016/j.jhydrol.2016.05.046>, 2016.

823 Essery, R.L.H., Rutter, N., Pomeroy, J., Baxter, R., Stahli, M., Gustafsson, D., Barr, A., Bartlett, P., Elder,
824 K.: SNOWMIP2: an evaluation of forest snow process simulations. Bull. Amer. Meteor. Soc.
825 90, 1120–1135, 2009.

826 [Eagleson, P.S.: Dynamic Hydrology, McGraw-Hill, 1970](#)

827 Foster, J.L., Sun, C., Walker, J.P., Kelly, R., Chang, A., Dong, J., Powell, H.: Quantifying the uncertainty
828 in passive microwave snow water equivalent observations. Remote Sens. Environ. 94, 187–
829 203, 2005.

830 Gan, Y., Zhang, Y., Kongoli, C., Grassotti, C., Liu, Y., Lee, Y. K., Seo, D. J.: Evaluation and blending of

831 ATMS and AMSR2 snow water equivalent retrievals over the conterminous United
832 States. *Remote Sens. Environ.* 254, 112280, 2021.

833 Gloege, L., Kornhuber, K., Skulovich, O., Pal, I., Zhou, S., Ciais, P., Gentine, P.: Land-Atmosphere Cascade
834 Fueled the 2020 Siberian Heatwave. *AGU Advances*, 3 (6), e2021AV000619, 2022.

835 Hamill, T.M., Whitaker, J.S., Snyder, C.: Distance-dependent filtering of background error covariance
836 estimates in an ensemble Kalman filter. *Mon. Weather Rev.* 129, 2776–2790, 2001.

837 Helfrich, S.R., McNamara, D., Ramsay, B.H., Baldwin, T., Kasheta, T.: Enhancements to, and forthcoming
838 developments in the interactive multisensor snow and ice mapping system (IMS). *Hydrol.*
839 *Process.* 21 (12), 1576–1586. <https://doi.org/10.1002/hyp.6720>, 2007.

840 Helmert, J., Şensoy Şorman, A., Montero, R.A., De Michele, C., De Rosnay, P., Dumont, M., Finger, D.,
841 Lange, M., Picard, G., Potopová, V., et al.: Review of Snow Data Assimilation Methods for
842 Hydrological, Land Surface, Meteorological and Climate Models: Results from a COST
843 HarmoSnow Survey. *Geoscience*, 8 (12), 489, 2018.

844 Houtekamer, P.L., Mitchell, H.L.: A sequential ensemble Kalman filter for atmospheric data
845 assimilation. *Mon. Weather Rev.* 129, 123–137, 2001.

846 [Huning, L.S., AghaKouchak, A.: Global snow drought hot spots and characteristics. *Proc. Natl. Acad. Sci.* 117\(33\), 19753-19759, 2020.](#)

847

848 Hunt, B.R., Kostelich, E.J., Szunyogh, I.: Efficient data assimilation for spatiotemporal chaos: a local
849 ensemble transform Kalman filter. *Phys. D Nonlinear Phenom.* 230, 112–126, 2007.

850 Imaoka, K., Kachi, M., Kasahara, M., Ito, N., Nakagawa, K., Oki, T.: Instrument performance and
851 calibration of AMSR-E and AMSR2. *Int. Arch. Photogramm. Remote. Sens. Spat. Inf. Sci.* 38
852 (8), 13–16, 2010.

853 Jeong, J.H., Linderholm, H.W., Woo, S.H., Folland, C., Kim, B.M., Kim, S.J., Chen, D.: Impacts of snow
854 initialization on subseasonal forecasts of surface air temperature for the cold season. *J.*
855 *Clim.* 26 (6), 1956–1972, 2013.

856 Kobayashi, S., Ota, Y., Harada, Y., Ebata, A., Moriya, M., Onoda, H., Onogi, K., Kamahori, H., Kobayashi,
857 C., Endo, H.: The JRA-55 reanalysis: general specifications and basic characteristics. *J.*
858 *Meteorol. Soc. Jpn. Ser. II* 93, 5–48, 2015.

859 Koster, R.D., Dirmeyer, P.A., Guo, Z., Bonan, G., Chan, E., Cox, P., Gordon, C.T., Kanae, S., Kowalczyk,
860 E., Lawrence, D., Liu, P., Lu, C.H., Malyshev, S., McAvaney, B., Mitchell, K., Mocko, D., Oki,
861 T., Oleson, K., Pitman, A., Sud, Y.C., Taylor, C.M., Verseghy, D., Vasic, R., Xue, Y., Yamada,
862 T., GLACE Team: Regions of strong coupling between soil moisture and
863 precipitation. *Science*, 305 (5687), 1138–
864 1140, <https://doi.org/10.1126/science.1100217>, 2004.

865 Koster, R.D., Mahanama, S., Yamada, T., Balsamo, G., Berg, A., Boisserie, M., Dirmeyer, P., Doblas-Reyes,
866 F., Drewitt, G., Gordon, C.: The second phase of the global land–atmosphere coupling
867 experiment: soil moisture contributions to subseasonal forecast skill. *J. Hydrometeorol.* 12,
868 805–822, 2011.

869 Kumar, S.V., Jasinski, M., Mocko, D.M., Rodell, M., Borak, J., Li, B., Beaudoin, H.K., Peters-Lidard, C.D.:

870 NCA-LDAS land analysis: development and performance of a multisensor, multivariate land
871 data assimilation system for the national climate assessment. *J. Hydrometeorol.* 20 (8), 1571–
872 1593. <https://doi.org/10.1175/JHM-D-17-0125.1>, 2019.

873 Kwon, Y., Yang, Z.-L., Hoar, T.J., Toure, A.M.: Improving the radiance assimilation performance in
874 estimating snow water storage across snow and land-cover types in North America. *J.*
875 *Hydrometeorol.* 18 (3), 651–668. <https://doi.org/10.1175/JHM-D-16-0102.1>, 2017.

876 Li, F., Orsolini, Y.J., Keenlyside, N., Shen, M.L., Counillon, F., Wang, Y.G.: Impact of snow initialization
877 in subseasonal-to-seasonal winter forecasts with the Norwegian Climate Prediction
878 Model. *J. Geophys. Res. Atmos.* 124 (17-18), 10033-10048, 2019.

879 Li, F., Wang, H.: Autumn Eurasian snow depth, autumn Arctic sea ice cover and East Asian winter
880 monsoon. *Int. J. Climatol.* 34(13), 3616-3625, 2014.

881 [Lim, S., Gim, H.J., Lee, E., Lee, S., Lee, W.Y., Lee, Y.H., Cassardo C., Park, S.K.: Optimization of snow-](#)
882 [related parameters in the Noah land surface model \(v3. 4.1\) using a micro-genetic algorithm](#)
883 [\(v1. 7a\). *Geosci. Model Dev.* 15\(22\), 8541-8559, 2022.](#)

884 Liu, Y., Peters-Lidard, C.D., Kumar, S.V., Arsenault, K.R., Mocko, D.M.: Blending satellite-based snow
885 depth products with in situ observations for streamflow predictions in the upper Colorado
886 River basin. *Water Resour. Res.* 51 (2), 1182–1202. <https://doi.org/10.1002/2014WR016606>,
887 2015.

888 Lee, Y.K., Kongoli, C., Key, J.: An in-depth evaluation of heritage algorithms for snow cover and snow
889 depth using AMSR-E and AMSR2 measurements. *J. Atmos. Ocean. Technol.* 32(12), 2319-
890 2336, 2015.

891 Meng, J., Yang, R., Wei, H., Ek, M., Gayno, G., Xie, P., Mitchell, K.: The land surface analysis in the
892 NCEP climate forecast system reanalysis. *J. Hydrometeorol.* doi:10.1175/JHM-D-11-090.1,
893 2012.

894 Meyal, A.Y., Versteeg, R., Alper, E., Johnson, D., Rodzianko, A., Franklin, M., Wainwright, H.: Automated
895 cloud based long short-term memory neural network based SWE prediction. *Front. Water*, 2,
896 574917, 2020.

897 Miyoshi, T., Yamane, S.: Local ensemble transform Kalman filtering with an AGCM at a T159/L48
898 resolution. *Mon. Weather Rev.* 135, 3841–3861, 2007.

899 Orsolini, Y.J., Senan, R., Balsamo, G., Doblas-Reyes, F.J., Vitart, F., Weisheimer, A., Carrasco, A., Benestad,
900 R.E.: Impact of snow initialization on sub-seasonal forecasts. *Clim. Dyn.* 41, 1969-1982, 2013.

901 [Orsolini, Y.J., Senan, R., Vitart, F., Weisheimer, A., Balsamo, G., Doblas-Reyes, F.: Influence of the](#)
902 [Eurasian snow on the negative North Atlantic Oscillation in subseasonal forecasts of the](#)
903 [cold winter 2009/10. *Clim. Dyn.* 47\(3-4\), 1325–1334. \[https://doi.org/10.1007/s00382-015-\]\(https://doi.org/10.1007/s00382-015-2903-8\)](#)
904 [2903-8, 2016.](#)

905 Overland, J. E., Wang, M.: The 2020 Siberian heat wave. *Int. J. Climatol.* 41, E2341-E2346, 2021.

906 Pullen, S., Jones, C., Rooney, G.: Using satellite-derived snow cover data to implement a snow analysis
907 in the met office NWP model. *J. Appl. Meteorol.* 50, 958–973. doi:10.1175/2010JAMC2527.1,
908 2011.

909 Pulliainen, J., Luojus, K., Derksen, C., Mudryk, L., Lemmetyinen, J., Salminen, M., Ikonen, J., Takala, M.,
910 Cohen, J., Smolander, T., Norberg, J.: Patterns and trends of Northern Hemisphere snow mass
911 from 1980 to 2018. *Nature*, 581 (7808), 294–298. [https://doi.org/10.1038/s41586-020-2258-](https://doi.org/10.1038/s41586-020-2258-0)
912 0, 2020.

913 Ramsay, B.H.: The interactive multisensor snow and ice mapping system. *Hydrol. Process.* 12 (10-11),
914 1537–1546, 1998.

915 Reichle, R.H.: Data assimilation methods in the Earth sciences. *Adv. Water Resour.* 31, 1411–1418,
916 2008.

917 Reichle, R.H., Draper, C.S., Liu, Q., Girotto, M., Mahanama, S.P., Koster, R.D., De Lannoy, G.J.:
918 Assessment of MERRA-2 land surface hydrology estimates. *J. Clim.* 30 (8), 2937-2960, 2017.

919 Reichle, R.H., Koster, R.D.: Bias reduction in short records of satellite soil moisture. *Geophys. Res. Lett.*
920 31, 2004.

921 Reichle, R.H., Koster, D., De Lannoy, G.J.M., Forman, B.A., Liu, Q., Mahanama, S.P.P., Toure, A.M.:
922 Assessment and Enhancement of MERRA Land Surface Hydrology Estimates. *J. Clim.* 24,
923 6322–6338, 2011.

924 Seo, E., Lee, M.I., [Jeong, J.H., Koster, R.D., Schubert, S.D., Kim, H.M., Kim, D.H., Kang H.S., Kim, H.K.,](#)
925 [MacLachlan, C., Scaife, A.A.: Impact of soil moisture initialization on boreal summer](#)
926 [subseasonal forecasts: mid-latitude surface air temperature and heat wave](#)
927 [events. *Clim. Dyn.* 52, 1695-1709, 2019.](#)

928 [Seo, E., Lee, M.I.,](#) Reichle, R.H.: Assimilation of SMAP and ASCAT soil moisture retrievals into the
929 JULES land surface model using the Local Ensemble Transform Kalman Filter. *Remote Sens.*
930 *Environ.* 253, 112222, 2021.

931 [Seo, E., Lee, M.I., Schubert, S.D., Koster, R.D., Kang, H.S.: Investigation of the 2016 Eurasia heat wave](#)
932 [as an event of the recent warming. *Environ. Res. Lett.* 15\(11\), 114018, 2020.](#)

933 Shlyueva, A., Tolstykh, M., Mizyak, V., Rogutov, V.: Local ensemble transform Kalman filter data
934 assimilation system for the global semi-Lagrangian atmospheric model. *Russ. J. Numer. Anal.*
935 *Math. Model.* 28(4), 419-442, 2013.

936

937 Sturm, M., Taras, B., Liston, G.E., Derksen, C., Jonas, T., Lea, J.: Estimating snow water equivalent using
938 snow depth data and climate classes. *J. Hydrometeor.* 11, 1380–1394, 2010.

939 Su, H., Yang, Z.-L., Dickinson, R.E., Wilson, C.R., Niu, G.-Y.: Multisensor snow data assimilation at the
940 continental scale: The value of gravity recovery and climate experiment terrestrial water
941 storage information. *J. Geophys. Res.*, 115, D10104, doi:10.1029/2009JD013035, 2010.

942 [Takala, M., Luojus, K., Pulliainen, J., Derksen, C., Lemmetyinen, J., Karna, J.P., Koskinen, J., Bojkov, B.:](#)
943 [Estimating northern hemisphere snow water equivalent for climate research through](#)
944 [assimilation of space-borne radiometer data and ground-based measurements. *Remote*](#)
945 [Sens. Environ.](#) 115:3517–3529, 2011.

946 Thomas, J.A., Berg, A.A., Merryfield, W.J.: Influence of snow and soil moisture initialization on sub-
947 seasonal predictability and forecast skill in boreal spring. *Clim. Dyn.* 47 (1), 49-65, 2016.

948 Toure, A.M., Luoju, K., Rodell, M., Beaudoin, H., Getirana, A.: Evaluation of simulated snow and
949 snowmelt timing in the Community Land Model using satellite-based products and
950 streamflow observations. *J. Adv. Model. Earth Syst.* 10(11), 2933-2951, 2018.

951 U.S. National Ice Center: IMS daily Northern Hemisphere snow and ice analysis at 1 km, 4 km, and
952 24 km resolutions, version 3. Boulder, Colorado, USA. NSIDC: National Snow and Ice Data
953 Center, accessed: 18 Aug 2022, <https://doi.org/10.7265/N52R3PMC>, 2008.

954 You, Y., Huang, C., Gu, J., Li, H., Hao, X., Hou, J.: Assessing snow simulation performance of typical
955 combination schemes within Noah-MP in northern Xinjiang, China. *J. Hydrol.* 581, 124380,
956 2020.

957

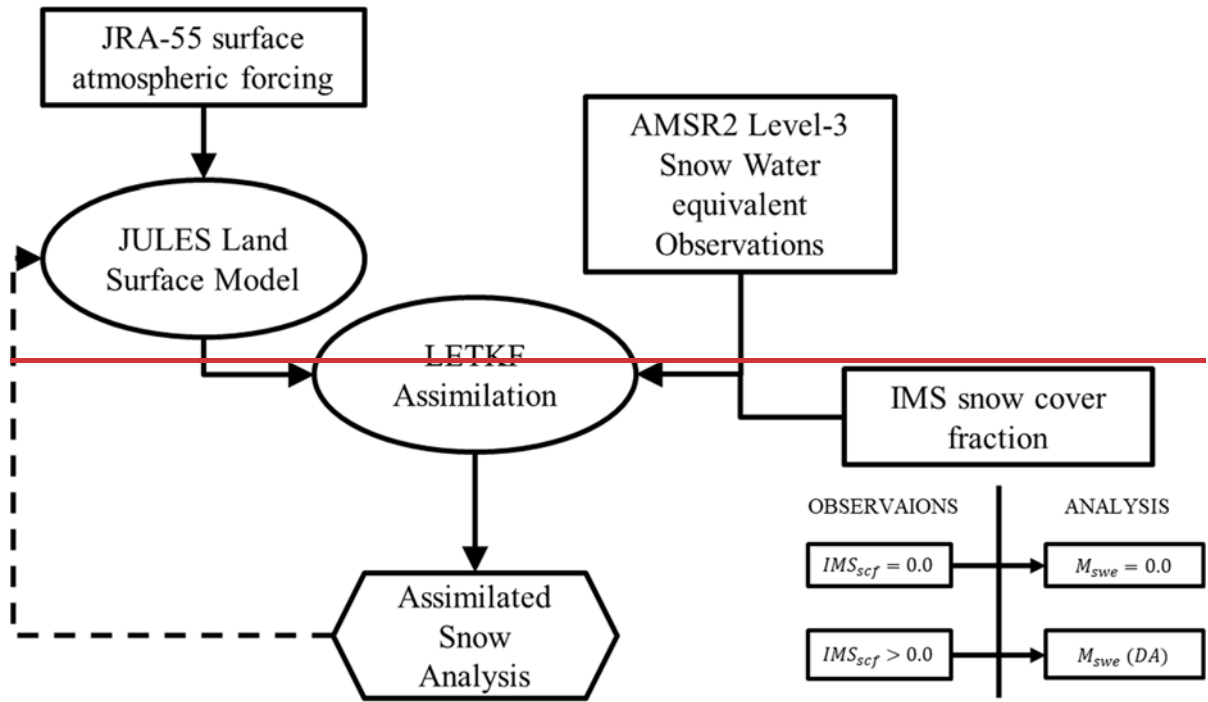
958 **Table 1.** Description of the land surface model, the data used, and assimilation experiment
 959 designs.

	INFORMATION	REFERENCES
Land Surface Model	JULES	Best et al., (2011)
Atmospheric Forcing	3-hourly JRA-55 reanalysis	Kobayashi et al., (2015)
Snow Observation	AMSR2 & IMS	Imaoka et al., (2010) Ramsay (1998) Helfrich et al., (2007)
Data Assimilation scheme	Local Ensemble Transform Kalman Filter (LETKF)	Hunt et al., (2007) Miyoshi and Yamane, (2007)
Resolution (km)	0.5° × 0.5° (~ 50)	
	1-day DA cycle	
Localization patch size (km)	3×3 (150), $\sigma = 30$	
Ensemble sizes	24	
Experiment period	2013-2020, APR	

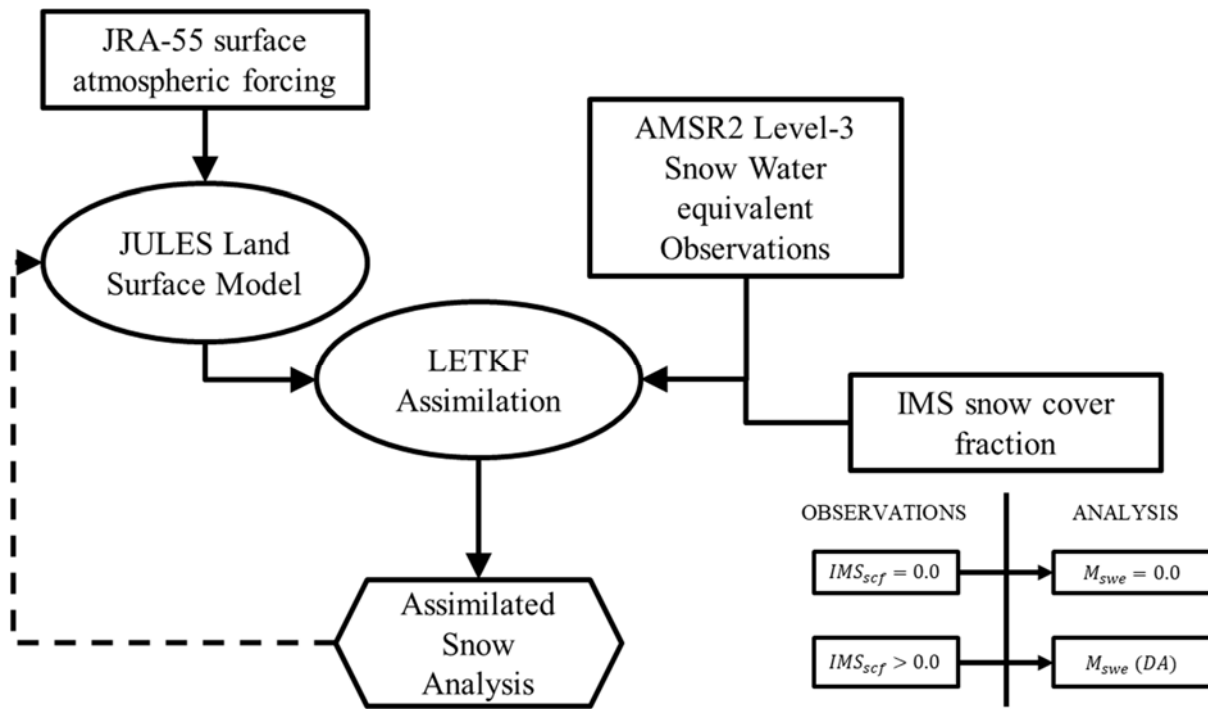
960

961

962



963



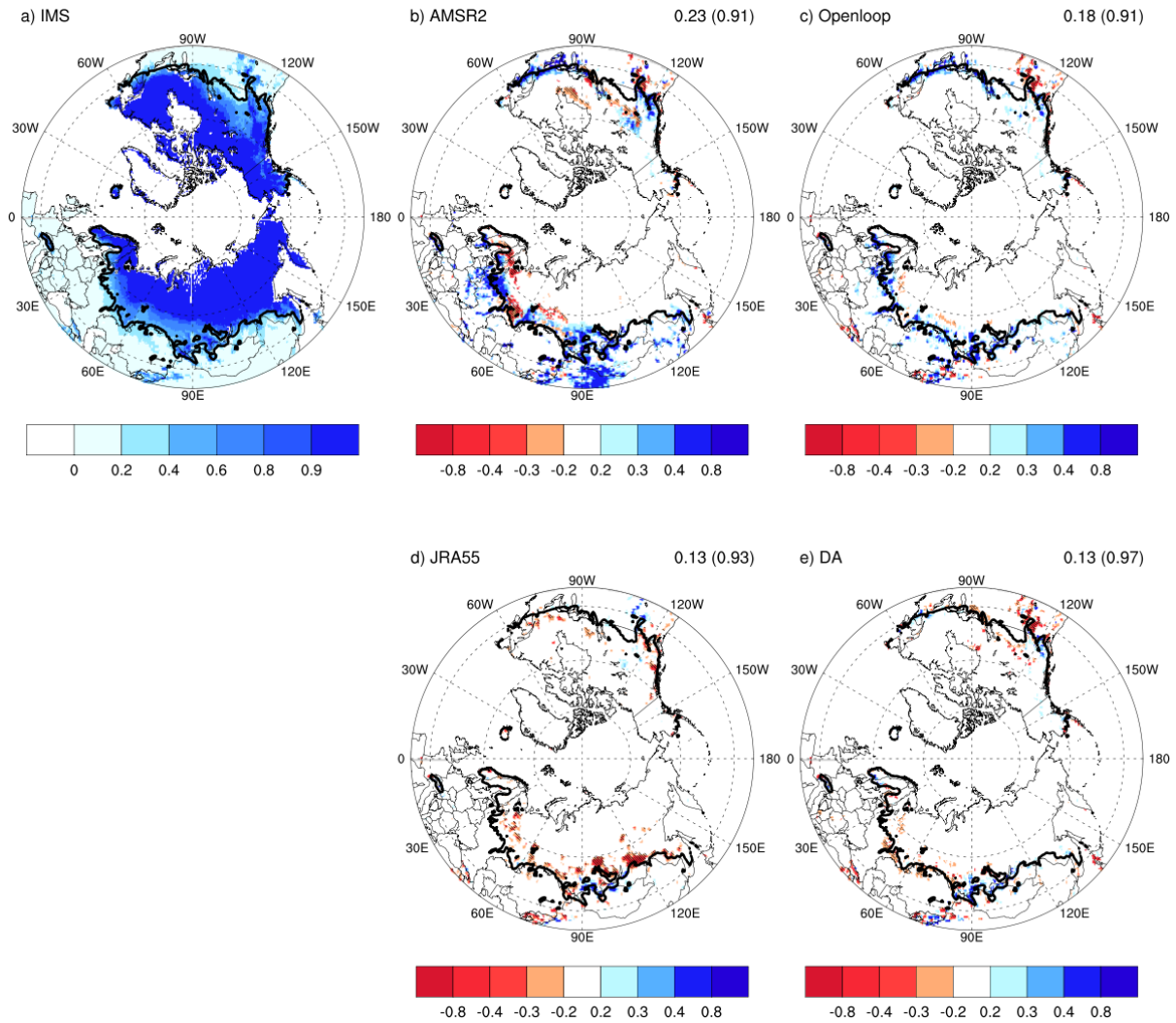
964

965 **Figure 1.** Schematic diagram of the snow assimilation system with satellite-derived

966 observations and the land surface model outputs.

967

968

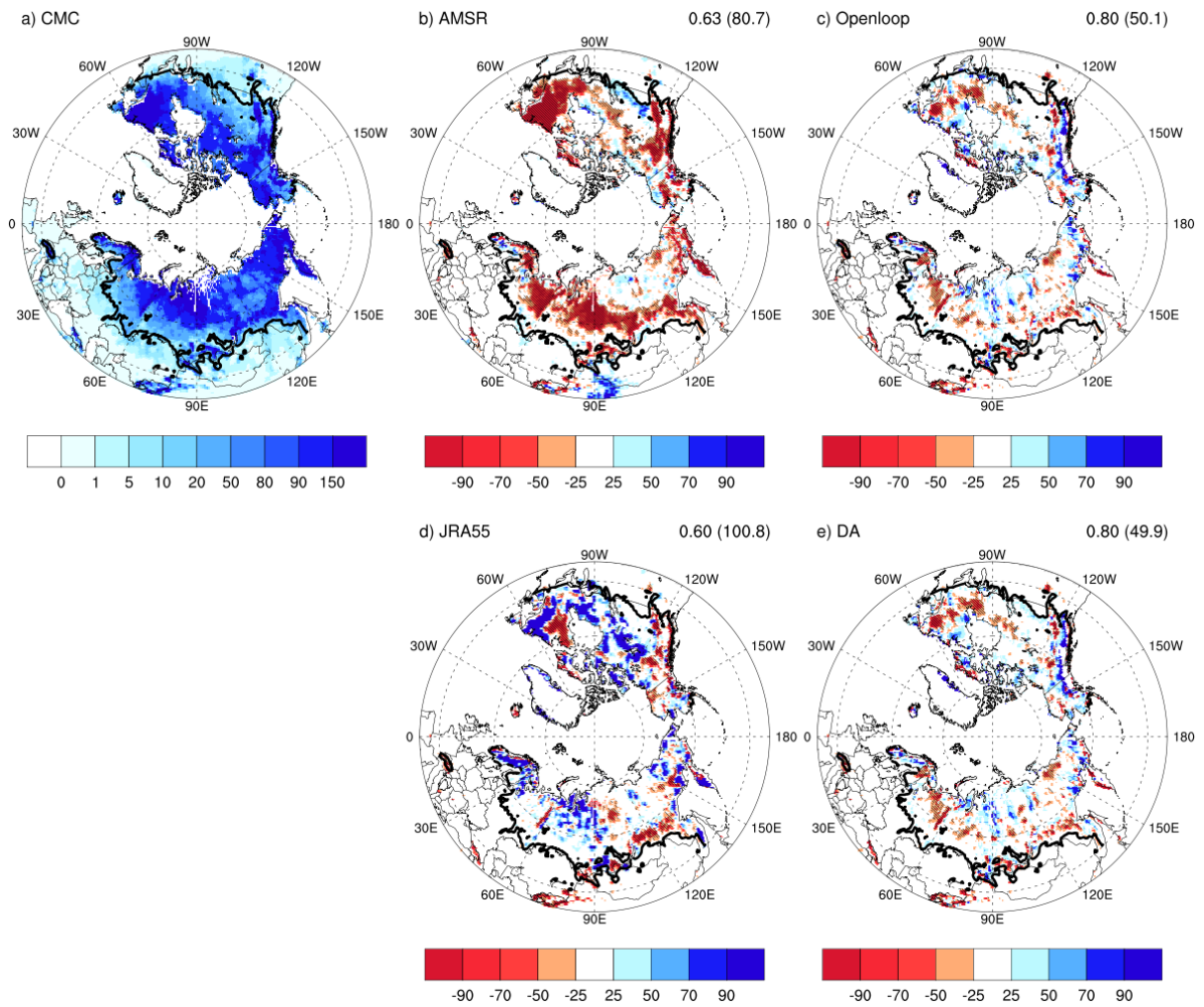


969

970 **Figure 2.** (a) Climatology of SCF from IMS used as reference and (b-e) the differences from
 971 IMS for AMSR2, base-line model simulation (Openloop), JRA55, and the data
 972 assimilation results (DA) for April during 2013-2020. The black line represents the
 973 boundary of the transition region, defined as the climatological-mean SWE of less than
 974 16mm. Each value on the top right is the root-mean-squared difference with IMS and
 975 the accuracy from IMS (parenthesis) for 15323 pixels over 40-60°N. The accuracy is
 976 defined in supplementary Table 1 as in previous study (Lee et al., 2015). Negative
 977 values in red shades are indicated with a diagonal line.

978

979

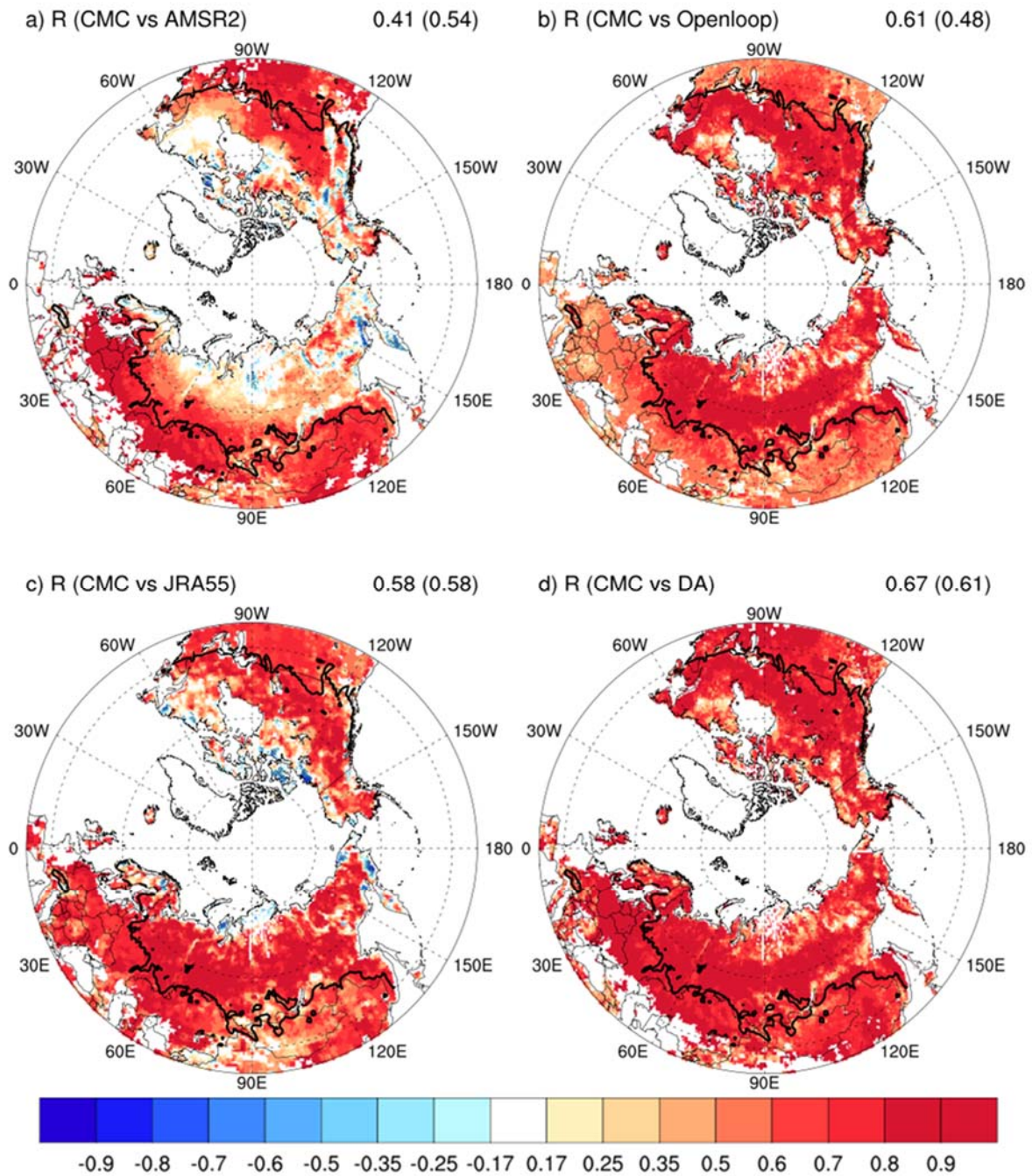


980

981 **Figure 3.** (a) Climatology of SWE from CMC used as reference and (b-e) the differences from
 982 CMC for AMSR2, base-line model simulation (Openloop), JRA55, and the data
 983 assimilation results (DA) for April during 2013-2020. The black line represents the
 984 boundary of the transition region, defined as the climatological-mean SWE of less than
 985 16mm. Each value on the top right is the pattern correlation with CMC for 26482 pixels
 986 over 40 °N and the root-mean-squared difference (unit: kg/m²) from ~~IMSCMC~~
 987 (parenthesis) for 15323 pixels over 40-60°N. Negative values in red shades are
 988 indicated with a diagonal line.

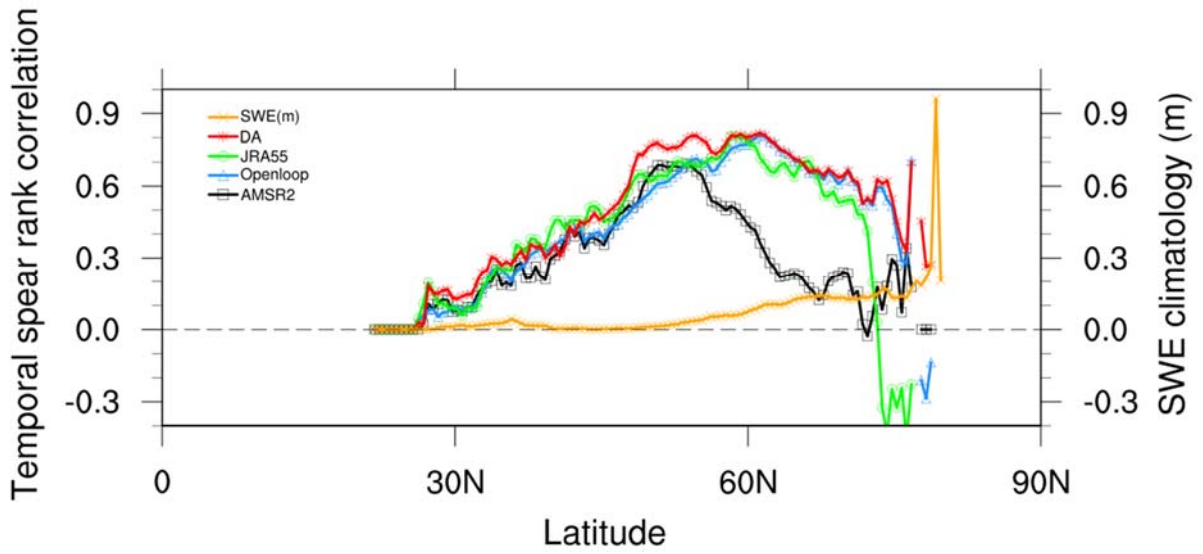
989

990



991

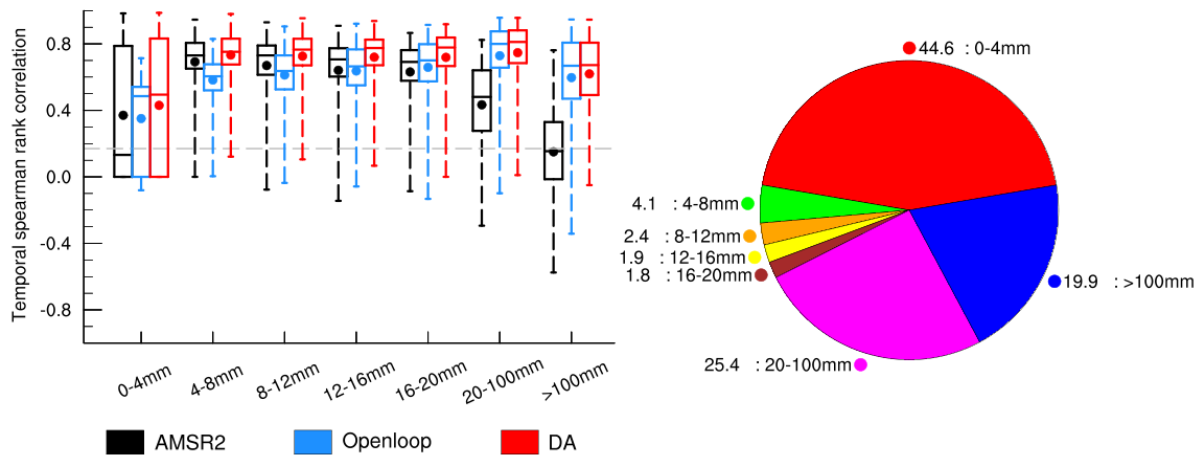
992 **Figure 4.** SWE skill measured as the Spearman rank correlation (R) with the CMC for AMSR2,
 993 base-line model simulation (Openloop), JRA55, and the data assimilation result (DA).
 994 The black line represents the boundary of the transition region, defined as the
 995 climatological-mean SWE of less than 16mm. Each value on the top is the area-average
 996 R of North hemisphere for 26482 pixels over 40°N and for 8801 pixels over the
 997 transition region (parenthesis). Negative values are indicated with a diagonal line.



998

999 **Figure 5.** Zonally-averaged Spearman rank correlation (R) along the latitude for SWE. The
 1000 yellow line indicates the climatology of SWE, and the black, blue, green, and red lines
 1001 denote the values of AMSR2, base-line model simulation (Openloop), JRA55, data
 1002 assimilation results (DA), respectively.

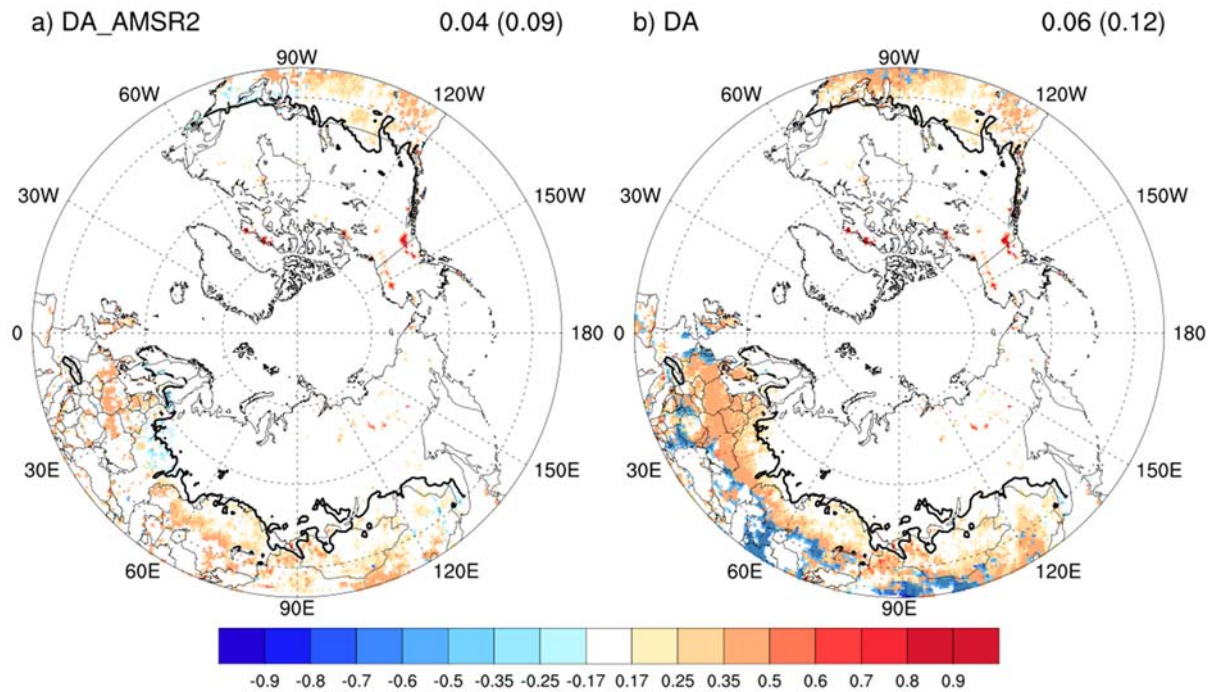
1003



1004

1005 **Figure 6.** Box plots of the Spearman rank correlation (R) according to SWE. The pie chart
 1006 shows the total area ratio (%) as a function of SWE amount. The black, blue, and red
 1007 boxes denote the AMSR2, base-line model simulation (Openloop), and the data
 1008 assimilation results (DA), respectively. The boxes indicate 25 and 75% percentiles, and
 1009 the line and point in the boxes shows the median and the mean values. The upper and
 1010 lower whiskers denote the 10 and 90% percentiles, respectively.

1011



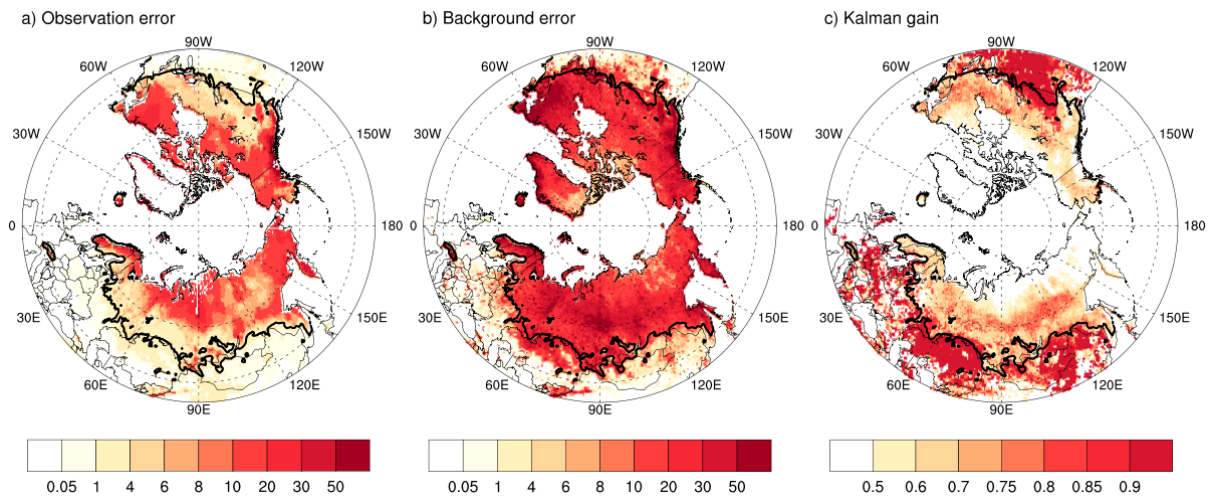
1012

1013 **Figure 7.** ~~Difference~~The difference in SWE skill, measured as the Spearman rank correlation
 1014 coefficient (R) with CMC₇, between the Openloop and the data assimilation ~~result~~results:
 1015 DA employing both AMSR2 and IMS (~~referred to as DA~~), as well as the data
 1016 ~~assimilation result~~and DA_AMSR2 utilizing solely AMSR2 and excluding IMS
 1017 (~~referred to as DA_AMSR2~~), for April during 2013-2020. The black line represents the
 1018 boundary of the transition region, defined as the climatological-mean SWE of less than
 1019 16mm. Each value on the top right is the area-average over 40°N and the transition
 1020 region (parenthesis). Negative values are indicated with a diagonal line.

1021

1022

1023



1024

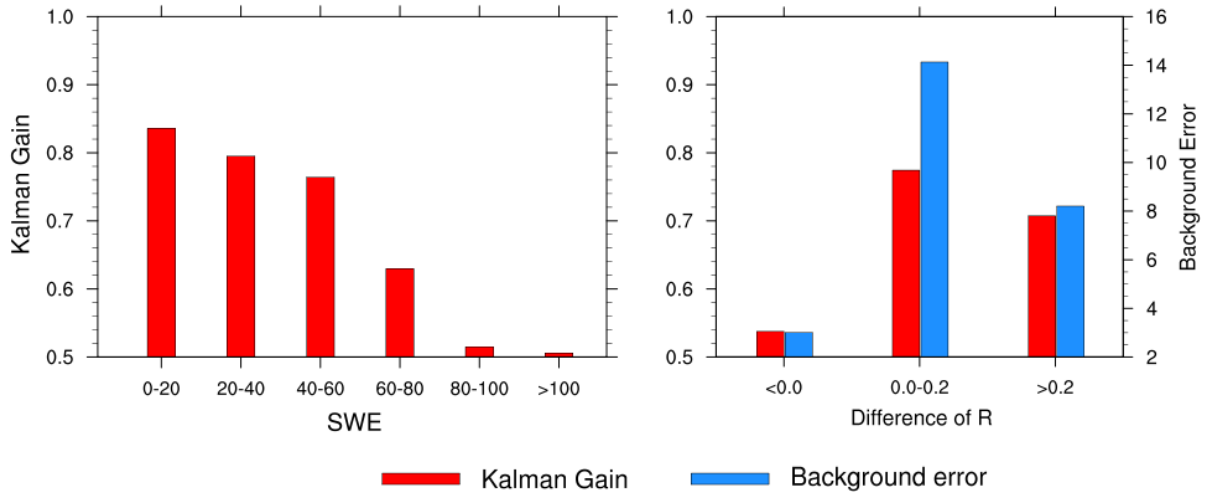
1025

1026

1027

1028

Figure 8. Spatial distribution of observation error, (unit: kg/m^2), background error, (unit: kg/m^2), and Kalman gain. The black line represents the boundary of the transition region, defined as the climatological-mean SWE of less than 16mm.



1029

1030

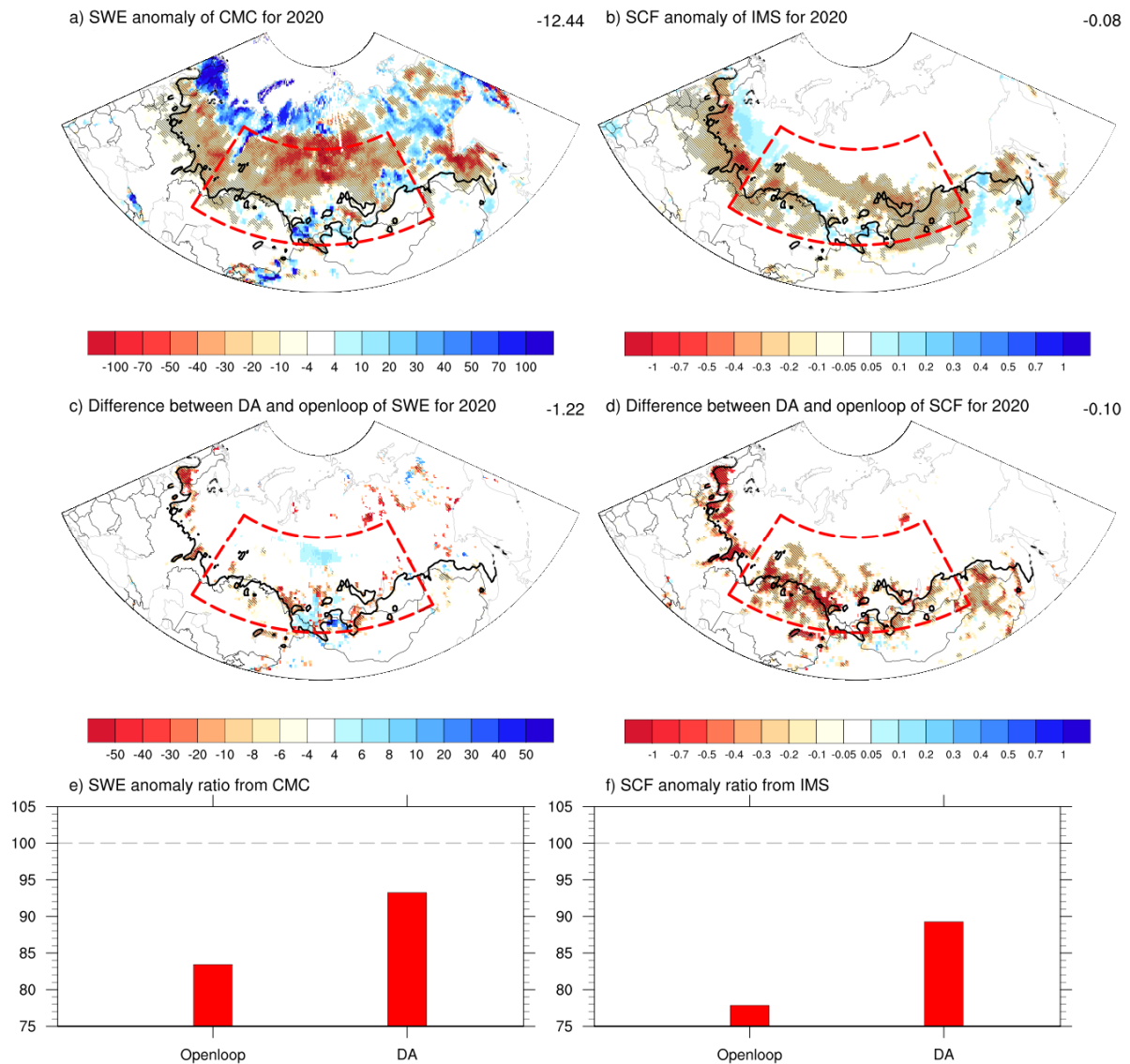
1031

1032

1033

1034

Figure 9. Bar chart of (left) the Kalman gain according to the SWE amount, and (right) the Kalman gain (red line) and background error (blue line) ~~according to~~ a function of the difference of the between Openloop and DA in Spearman rank correlation coefficient (R) between Openloop and DA.



1035

1036

1037

1038

1039

1040

1041

1042

1043

Figure 10. Anomalies of a) SWE from CMC and b) SCF from IMS as well as the difference (c, d) of variables between DA and openloop in April 2020. Bar chart (e, f) indicates the ratio of DA and openloop to verification data such as CMC and IMS in the red box (48–65°N and 55–120°E), which is the region associated with extreme high-temperature events, focused on this study. Negative values are indicated with a diagonal line.